Laminar, transitional and turbulent annular flow of drag-reducing polymer solutions

A. Japper-Jaafar [a,b], M.P. Escudier [b], R.J. Poole [b,*]

[a] Mechanical Engineering Department, Universiti Teknologi Petronas, 31750 Tronoh, Perak, Malaysia
[b] Department of Engineering, University of Liverpool, Brownlow Street, Liverpool L69 3GH, Merseyside, United Kingdom

ARTICLE INFO

ABSTRACT

Mean and rms axial velocity-profile data obtained using laser Doppler anemometry are presented together with pressure-drop data for the flow through a concentric annulus (radius ratio $\kappa = 0.506$) of a Newtonian (a glycerine–water mixture) and non-Newtonian fluids—a semi-rigid shear-thinning polymer (a xanthan gum) and a polymer known to exhibit a yield stress (carbopol). A wider range of Reynolds numbers for the transitional flow regime is observed for the more shear-thinning fluids. In marked contrast to the Newtonian fluid, the higher shear stress on the inner wall compared to the outer wall does not lead to earlier transition for the non-Newtonian fluids where more turbulent activity is observed in the outer wall region. The mean axial velocity profiles show a slight shift ($\sim$5%) of the location of the maximum velocity towards the outer pipe wall within the transitional regime only for the Newtonian fluid.

1. Introduction

The study of fluid flowing through an annulus has been the subject of interest since the early work by Rothfus et al. [1] which concerned a Newtonian fluid. Annular flow of a non-Newtonian fluid has a number of engineering applications, especially in the oil industry where the drilling fluid (or 'mud') is pumped down the drill string, through the drill bit and finally up the annulus, during the oil and gas drilling process. There are also other applications such as in the food, chemical and pharmaceutical industries, that involve non-Newtonian fluids flowing through annular pipes [2].

Newtonian and non-Newtonian fluid flow in a circular pipe is symmetrical in the laminar and fully-turbulent regimes [3–7]. In such cases the positions of zero shear stress and maximum velocity coincide. In the transitional-flow regime, however, while the flow of Newtonian fluids remains symmetrical on average, strong asymmetry has been observed for a wide range of non-Newtonian fluids [6,8–12]. In contrast with the pipe-flow situation, fully-developed annular flow in the laminar and turbulent regimes involves a combination of two boundary layers extending from the pipe walls to a point of maximum velocity which does not lie in the centre of the annular gap. The two boundary layers are of different thicknesses and possibly of different flow regimes due to the different degrees

of curvature of the inner and outer pipe walls [13]. As a result of the interaction of these two layers the flow is then asymmetric. Hence, in this type of flow, the position of zero shear stress will not, in general, be coincident with the position of maximum velocity. It is also the case that turbulent transport phenomena are expected to differ from those of symmetric flows in circular pipes [14–16].

Early investigations for the flow of Newtonian fluids by Knudsen and Katz [17], Rothfus et al. [1,18], Walker and Rothfus [19] and Brighton and Jones [20] assumed coincidence of the position of zero shear stress and maximum velocity. Lawn and Elliott [21] were the first to show, using hot-wire anemometry, that the positions of zero shear stress and maximum velocity for fully-developed turbulent flow are non-coincident. They found that for radius ratios κ less than 0.4 the position of zero shear stress was closer to the inner pipe wall than that of the maximum velocity. The inner velocity profiles were also found to deviate from the well-known log law (derived from pipe-flow data). Their findings were later supported by Rehme [14,22] who studied fully-developed turbulent flow of air using hot wire anemometry in concentric annuli of varying radius ratios ($\kappa = 0.02$, 0.04 and 0.1). Nouri et al. [15] were the first authors to employ laser Doppler anemometry (LDA) for both Newtonian and non-Newtonian annular-flow measurements ($Re \geq 8900$ for Newtonian and $Re \geq 1150$ for non-Newtonian flows). They measured the Reynolds shear stress of a Newtonian fluid in an annulus of radius ratio of 0.5 and found that within their experimental uncertainty the location of zero shear stress could not be distinguished from that of the maximum velocity. These positions were found to be closer to the inner pipe wall and independent of

Nomenclature

a	Carreau–Yasuda parameter
A	Cross-sectional area (m^2)
b	Diameter of CaBER plates (4 mm)
c	Polymer concentration (%, w/w)
D_{CaBER}	Filament diameter in CaBER (mm)
D_o	Midpoint filament diameter in CaBER following cessation of stretch deformation (mm)
DR	Drag reduction (%) ($\equiv ((f_n - f_p)/f_n) \times 100$)
f	Fanning friction factor ($\equiv 2\tau_W/\rho U_B^2$)
h	Distance between plates in CaBER (mm)
HB	Herschel–Bulkley number ($\equiv \tau_y/K(U_B/R)^n$)
k	Power law consistency index (Pa s^n)
K	Herschel–Bulkley consistency index (Pa s^n)
L	Pipe length over which the pressure drop was measured (m)
m	Slope of linear fitting to CaBER data (mm/s)
n	Power-law exponent
p	Pressure (Pa)
Δp	Pressure drop (Pa)
P	Wetted perimeter (m)
Q	Volumetric flow rate (m^3/s)
r	Radial location (m)
R	Pipe radius (m)
r_{max}	Point of maximum velocity (m)
r_p	Extent of plug region (m)
$r_{\tau=0}$	Radial location of zero shear stress (m)
Re	Reynolds number based on viscosity at the wall ($\equiv \rho U_B D_H/\eta_W$)
Re_{crit}	Critical Reynolds number obtained from time traces of the mean axial velocity
Re_1	First Reynolds number limit representing onset of transition
Re_2	Second Reynolds number limit representing offset of transition
t	Time (s)
T_B	Filament break-up time in CaBER (s)
Tr	Trouton ratio $\left(\equiv \eta_E(\sqrt{3}\dot{\varepsilon})/\eta(\dot{\gamma}) \right)$
u	Mean axial velocity (m/s)
u_τ	Friction velocity (m/s) $\left(\equiv \sqrt{\tau_W/\rho} \right)$
u'	rms axial velocity fluctuation (m/s)
U_B	Bulk velocity (m/s) ($\equiv Q/(\pi(R_0^2 - R_0^2))$)
U_{local}	Local mean velocity (m/s)
U_{max}	Maximum velocity (m/s)
v'	rms radial velocity fluctuation (m/s)
w'	rms tangential velocity fluctuation (m/s)
y	Distance from pipe wall (m)

Greek letters

β	Time ratio
$\dot{\varepsilon}$	Strain rate determined from CaBER (1/s) ($\equiv -(4/D_o)(dD_{CaBER}/dt)$)
$\dot{\gamma}$	Shear rate (1/s)
η	Shear viscosity (Pa s)
η_E	Uniaxial extensional viscosity (Pa s)
η_o	Zero-shear rate viscosity (Pa s)
η_W	Wall shear viscosity obtained from τ_W and $\dot{\gamma}_W$ via Carreau–Yasuda fit (Pa s)
η_∞	Infinite-shear rate viscosity (Pa s)
κ	Radius ratio, ($\equiv R_i/R_o$)
λ	Characteristic relaxation time in CaBER (s)
λ_{CY}	Carreau–Yasuda constant representing onset of shear thinning (s)
ρ	Fluid density (kg/m^3)
$\rho\overline{u'v'}$	Reynolds shear stress (Pa)
τ	Stress (Pa)
τ_A	Average wall shear stress (Pa)
τ_W	Wall shear stress (Pa) ($\equiv \Delta pD/4L$)
τ_y	Apparent yield stress (Pa)
ξ	Non-dimensional radial location in annulus ($\equiv (r - R_i)/(R_o - R_i)$)

Subscripts

H	Hydraulic
i	Inner pipe
max	Maximum
n	Newtonian
o	Outer pipe
p	Polymer
W	Wall

Superscripts

$+$	"wall" coordinates

the Reynolds number. In wall coordinates, the inner and outer wall profiles of Newtonian flows were found to obey the well-known log law. However, due to opacity of the non-Newtonian fluid used, carboxymethylcellulose (CMC), the Reynolds shear stress could not be measured and therefore maximum velocity and zero shear stress coincidence was assumed. By performing Direct Numerical Simulations of turbulent concentric annular flow of a Newtonian fluid for radius ratios of 0.1 and 0.5 at $Re = 8900$, Chung et al. [16] confirmed that the positions of zero shear stress are closer to the inner wall than those of the maximum velocity for both radius ratios though in the $\kappa = 0.1$ geometry the effect is more severe.

Escudier et al. [23] performed LDA measurements together with numerical simulations of a shear-thinning fluid, a xanthan gum/carboxymethylcellulose mixture, in a concentric annulus of radius ratio 0.506 within the laminar-flow regime. The velocity profiles were again observed to be skewed towards the inner pipe of the annulus. The calculated velocity distributions using the power-law fluid as a model, were found to be slightly flatter with reduced peak velocity levels (when normalised with the bulk velocity U_B) when compared to the Newtonian fluid flow. Escudier et al. [24] conducted LDA measurements of three different non-Newtonian fluids – a xanthan gum, a carboxymethylcellulose and a laponite–carboxymethylcellulose blend – within the laminar, transitional and turbulent annular flow regimes ($\kappa = 0.506$). Measurements were also conducted on a control Newtonian fluid, a glycerine–water mixture. In turbulent flow, at drag-reduction levels greater than 35%, an upward shift of the universal velocity profile was observed with a slope greater than that of the log law. A slight increase in the peak of the axial rms fluctuation component, normalized with U_B, compared to the Newtonian value was seen while the tangential component of fluctuation was distributed almost uniformly across the annular gap and significantly below the Newtonian values.

A number of studies have specifically investigated transitional flow of Newtonian fluids in annular flow. Rothfus et al. [1] undertook such a study using air flowing through annuli with two-different radius ratios ($\kappa = 0.162$ and 0.650) for a moderate Reynolds number range ($1250 \leq Re \leq 21,600$). Using a pitot tube to measure the velocities, it was found that the position of maximum velocity is the same for laminar and turbulent flow in both annuli. However,
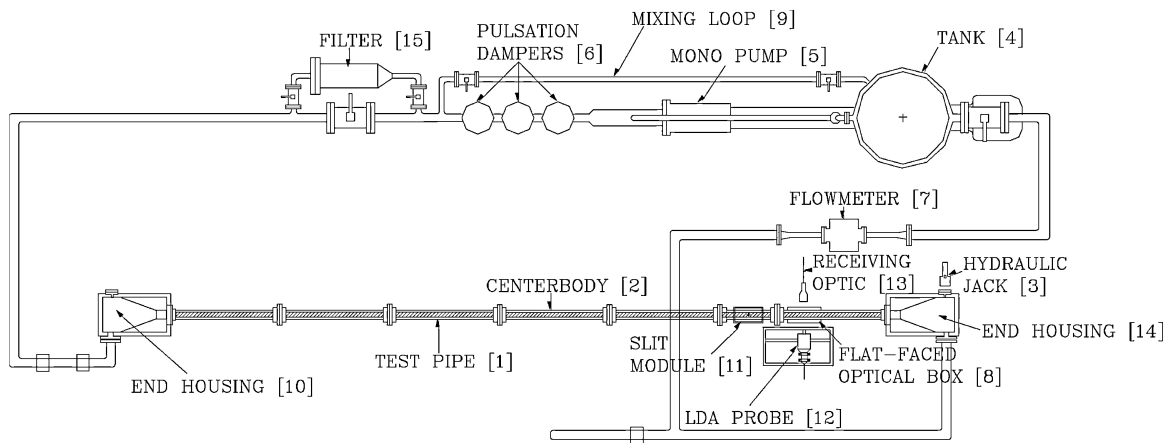
Fig. 1. Schematic diagram of the annular pipe-flow loop (flow direction is anti-clockwise).

within the transitional regime the position is shifted closer to the inner pipe. The extent of the Reynolds-number range for the transitional regime was found to be a function of the radius ratio and appeared to be wider than for pipe flow.

Walker and Rothfus [19] also used a pitot tube to study the behaviour of the radial location of maximum velocity r_{max}, with Reynolds number for water flowing in an annulus ($\kappa = 0.331$). The authors discovered that r_{max} in fully-turbulent flow corresponds to that in laminar flow. During transition the values of r_{max} obtained from the velocity profiles start to deviate from the laminar flow position at $Re = 650$. In the early transitional regime, r_{max} appears to shift towards the inner pipe wall and then reverses its location as the Reynolds number is further increased. The outward progression of r_{max} continues past beyond the laminar-flow value with increasing Reynolds number and stops only when a critical Reynolds number of 2200 is attained. As Reynolds number increases further r_{max} re-approaches its laminar value.

Hanks and Bonner [13] performed a theoretical analysis on the stability of laminar Newtonian flow within a concentric annulus. Their theory predicts that the inner flow region is the least stable of the two flow regions and will undergo transition to turbulence while the flow in the outer region remains laminar. Consequently, the wall shear stress on the inner surface will increase significantly due to the change in the momentum-transport mechanism to a turbulent mode. The increase in wall shear stress leads to a shift in the radial location of the maximum velocity to a higher value, towards the outer wall. The radial location of the maximum velocity will reach a maximum once the outer flow region undergoes transition to turbulence. Beyond this critical Reynolds number the radial location of maximum velocity will decrease to a value corresponding to that in turbulent flow where $r_{max,turbulent} < r_{max,laminar}$.

Unlike the situation for Newtonian fluid flow, there is a very limited literature of experiment and stability analysis within the transitional flow regime for non-Newtonian fluids. Amongst the available literature, Escudier et al. [24] monitored the axial turbulence intensity of Newtonian and non-Newtonian fluid flows (xanthan gum, carboxymethylcellulose and a laponite/carboxymethylcellulose mixture) at the centre of the annular gap as a means of identifying the onset of transitional flow. Although departure from the laminar-flow regime was observed for the friction factor, f against the Reynolds number, $Re(\equiv \rho U_B D_H / \eta_W)$ plot, a sudden increase above the noise level in the normalized axial turbulence intensity, u'/U_B, was detected at a slightly lower Reynolds number than what was observed on the f–Re plot for all the fluids studied. Despite the circumferential asymmetry highlighted by the authors, the mean axial velocity distribution for the Newtonian control case showed a slight shift of the location

of maximum velocity towards the outer wall within the transitional regime, a trend which was absent for the non-Newtonian fluid flows.

Gucuyener and Mehmetoglu [25] applied Hanks' stability criterion [13] to shear-thinning and yield-stress fluids. Using the modified Reynolds number (based on an equivalent diameter and characteristic parameters of the flow) the authors found that, regardless of the fluid rheology, two very distinct critical Reynolds number are obtained in a concentric annulus. They claim that the inner flow region will always have a lower critical Reynolds number value compared to the outer flow region. Mishra and Mishra [26], however, predicted only one critical Reynolds number for the transition to turbulence using Mishra and Tripathi's criterion [27] for power-law fluids. This critical Reynolds number is found to be an increasing function of the radius ratio. Transition to turbulence is also predicted to be delayed with increased shear-thinning (i.e. decreasing power-law index).

What is clear from the foregoing is that there is currently no complete and detailed experimental data set in the literature, using reliable measurements techniques (for example laser-based techniques such as LDA or particle image velocimetry), of the mean flow and turbulence structure (e.g. u' v', w' and the Reynolds shear stress) for transitional and turbulent flows within an annular pipe for non-Newtonian fluids. To address this deficit in the current study we have conducted detailed LDA measurements in an annular pipe within the three flow regimes (i.e. laminar, transitional and fully turbulent) with particular attention placed on the transitional flow region and the drag-reducing behaviour of a semi-rigid polymer solution, xanthan gum. The transitional flow regime is studied by monitoring the axial rms fluctuation level at fixed radial locations close to the inner and outer walls ($\xi = 0.1$ and 0.9) and the time traces of the mean axial velocity at these locations. Laminar and transitional measurements are also performed for an additional polymer, carbopol, which is known to exhibit a yield stress.

2. Experimental arrangement

A 5.81-m long annular-flow facility, essentially a modified version of the facility described in detail in Escudier et al. [24], was utilized as shown in Fig. 1. The test pipe [1] comprised four 1041 mm long, one 625 mm long and one 718 mm long precision-bore borosilicate glass tubes, with an average internal diameter of 100.4 ± 0.1 mm and wall thickness of 5 ± 0.1 mm. The inner centrebody [2] was made of thin-walled stainless steel tube with an outside diameter of 50.8 mm giving a radius ratio, $\kappa = 0.506$ and a length-to-hydraulic diameter ratio of 117. The thin wall thickness of the centrebody gave a near neutral buoyancy in a
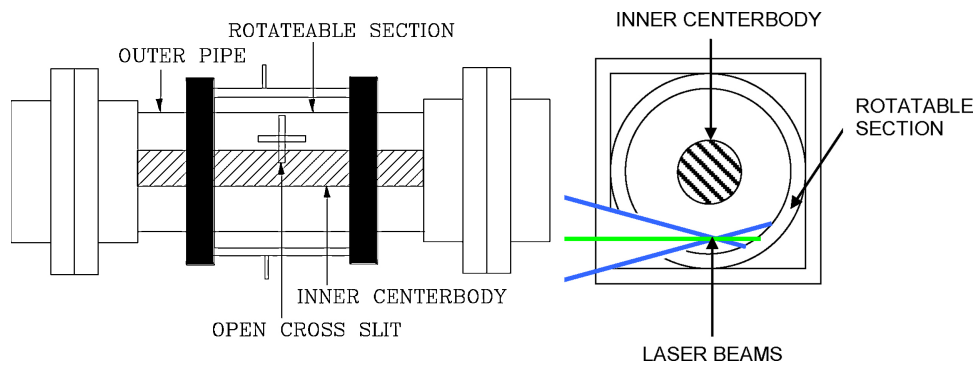
Fig. 2. Schematic of the slit module.

water-based solution, minimizing hog and sag; i.e. the possibility of the centrebody to arch upwards or downwards is reduced. The centrebody was held in position by a thrust bearing located in the upstream end and a hydraulic jack [3] tensioned to 3 tonnes axial load on the downstream end of the annulus. The fluid was driven from a 500 l capacity stainless steel tank [4] by a positive-displacement progressive-cavity pump [5] (Mono-type, E101 with a maximum flowrate of 0.025 m^3/s) with three pulsation dampers [6] to smooth the flow. A Fischer and Porter MAG-SM Series 1000 electromagnetic flowmeter (model 10D1) with a maximum capacity of 0.0333 m^3/s [7] was also incorporated in the experimental facility. The temperature of the fluid was monitored using a platinum resistance thermometer positioned inside the tank with an accuracy of $\pm 0.1\,°C$. During a run the temperature of the fluid in the rig never varied by more than 1 °C.

Pressure-drop measurements were conducted using a differential pressure (transducer GE Druck type LPX9381), between tappings at $75.8D_H$ downstream of the inlet to the pipe test and $117.1D_H$. Velocity profiles and Reynolds stress measurements were conducted using a Dantec Fiberflow laser Doppler anemometry (LDA) system comprising of a 60X10 probe and a Dantec 55X12 beam expander together with Dantec Burst Spectrum Analyzer signal processors (model 57N10 and 57N20). The lens focal length is 160 mm and the measured half angle between the laser beams is 9.14° which produces a measuring volume with a diameter of 36 μm and a length of 0.22 mm in air. Profiles of mean velocity (u) and rms Reynolds normal stress (u', v' and w') were performed at a location $104.7D_H$ downstream of the inlet. Poole [28] has established that for radius ratios $\kappa \geq 0.5$, the required development length for laminar Newtonian flow is equal to that of the equivalent channel flow; e.g. a development length of about $88D_H$ is required for $Re = 2000$. As the development length for turbulent flow is significantly lower than that for laminar flow [29,30], we consider that the distance from the inlet to the location of measurements is more than sufficient for the flow to reach fully-developed conditions. A water-filled flat faced optical box [8] installed at the measurement location was used to minimise the refraction of the laser beams making it possible to obtain data closer to the outer pipe wall where refraction is most severe due to the curved pipe wall. The velocity measurements and the respective radial locations were corrected using the ray-tracing method outlined by Presti [31]. For some measurements a "slit module" [11] was also used. This module is shown in Fig. 2 and was adapted from the arrangement first used by Poggi et al. [32] and more recently by Escudier et al. [5]. It consists here of an open cross slit on the outer pipe of the annulus which allows both pairs of laser beams to have the same optical path without any refraction thus providing a means of measuring two velocity components (axial and radial) simultaneously using LDA and permitting the determination of the Reynolds shear stress ($\rho \overline{u'v'}$). A flat-faced box was constructed around the outer pipe with the cross

slit to prevent leakage through the slit. The openings of the cross slit were constructed to be as small as possible to minimise disturbance to the flow but sufficient to permit the laser beams to pass through.

At each location across the annular gap, 10,000–30,000 data samples were collected and processed using a simple ensemble-averaging method. Processing the data using a transit-time weighting method [33], to account for velocity-biasing effects, produced minimal differences (average of ∼2% in the turbulence component). A maximum statistical error, for a 95% confidence interval, was less than 0.5% in mean velocity and less than 1.5% in the turbulence intensity based on the method of Yanta and Smith [34]. The flowrates obtained from integration of the LDA mean velocity profiles were found to be within 1.5% of the value provided by the flowmeter.

3. Working fluid preparation and characterisation

As Newtonian control fluids, we used both water and a glycerine–water solution. The latter was prepared by first adding the 60% (weight) glycerine into the 500 l tank. Water was then added until the total volume of fluid was sufficient to fully fill the rig (∼500 l) during pump operation. The solution was circulated around the whole flow loop until homogeneity was achieved which was determined by measuring the viscosity of the fluid collected from the flow loop every 30 min. The final glycerine–water mixture had a density of 1070 kg/m^3 and a shear viscosity, measured at 20 °C, of 38.6 mPa s.

The first of the two polymers used here was xanthan gum (Ketrol TF) obtained in powder form from Kelco Co. with the molecular weight of an individual xanthan gum chain reported by the supplier to be in excess of 10^6 g/mol. A quantity of approximately 700 l of tap water was used as the solvent for the polymer. Prior to the addition of polymer powder, water was circulated within the facility to remove any dissolved air. Mixing of part of the solvent with the powder was achieved by circulating the polymer solution within the mixing loop [9] at a low pump speed for at least 5 h before the mixing loop was opened and the solution circulated in the flow loop, allowing further mixing with the rest of the solvent in the pipe for at least another 5 h, until the solutions were visibly homogeneous. The homogeneity of each solution was also checked by comparing the viscometric data with a small sample solution (∼500 ml) of the same concentration prepared separately. To retard bacteriological degradation, 37% (w/w) formaldehyde was added to the polymer solutions at a concentration of 100 ppm. The polymer solution was left to hydrate in the rig for at least 24 h prior to the LDA measurements.

Steady-shear measurements were conducted at 20 °C on small sample solutions (∼500 ml) of xanthan gum prepared separately outside the flow loop for concentrations in the range 0.01–0.75%
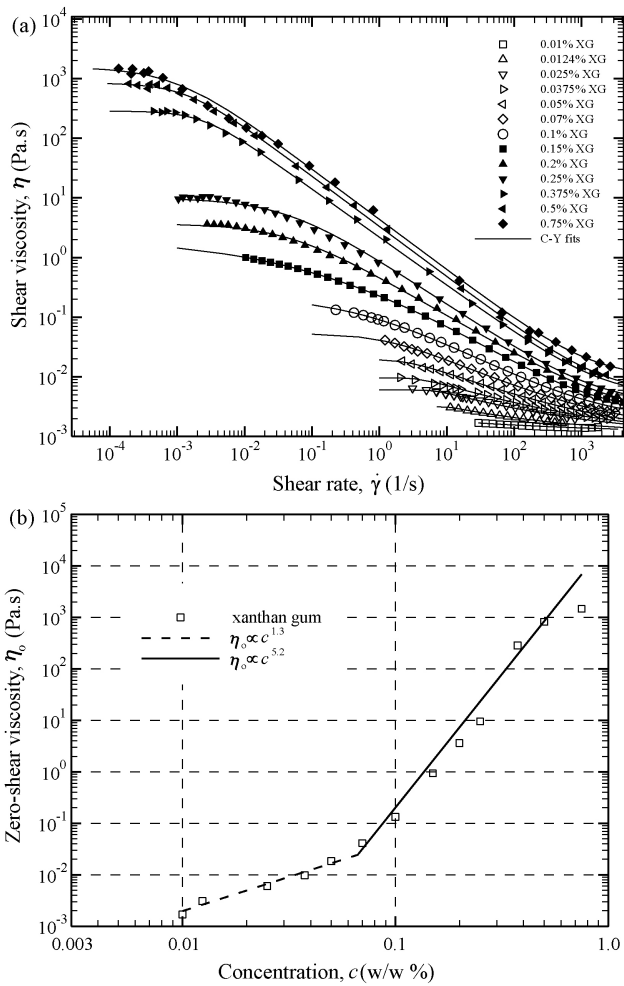
Fig. 3. (a) Viscometric data for xanthan gum solutions together with the Carreau–Yasuda fits. (b) Zero-shear viscosity versus concentration for xanthan gum at 20 °C.

(w/w) using a TA-Instruments Rheolyst AR 1000N controlled-stress rheometer. For low concentrations ($\leq$0.1%) a 41.2 mm mean diameter double concentric cylinder was used while for the higher concentrations a 40-mm, 2° cone-and-plate geometry were utilized. The plot of shear viscosity against shear rate for xanthan gum in Fig. 3(a) shows increased dependence of the shear viscosity, η on shear rate, $\dot{\gamma}$ with increasing concentration i.e. increased shear-thinning. The Carreau–Yasuda model [35] was used to fit the data:

$$\frac{\eta - \eta_o}{\eta_o - \eta_\infty} = \frac{1}{[1 + (\lambda_{CY}\dot{\gamma})^a]^{n/a}} \tag{1}$$

where η_o and η_∞ are the viscosities in the zero-shear and infinite-shear plateaus while λ_{CY}, n and a are constants which, respectively, represent the inverse shear rate at the onset of shear thinning, the power-law index and a fitting parameter introduced by Yasuda et al. The fits were achieved using the methodology outlined in Escudier et al. [36] and the parameter values are provided in Table 1. From Fig. 3(b), a log-log plot of zero-shear viscosity versus concentration for xanthan gum, the slope was found to be about 1.4 for the semi-dilute non-entangled region (i.e. below a critical concentration) and 5.2 for the entangled region. These values agree well with values available in the literature [37–39]. The location of the critical concentration for the formation of a polymeric network was found to be about 0.067%.

Although only possible for concentrations higher than those used in the fluid-dynamic measurements ($c \geq 0.2\%$, w/w), extensional property measurements were possible for xanthan gum and were carried out using a Capillary Break-up Extensional Rheometer ("CaBER") supplied by Thermo Electron GmbH in conjunction with a high-speed camera. The CaBER utilizes a laser micrometer, with a resolution of around 10 μm, to monitor the diameter of the thinning elongated filament, which evolves under the action of viscous, inertia, gravitational and elastocapillary forces. High-speed digital imaging of the process was captured by a Dantec Dynamics Nano Sense MKIII high-speed camera with a Nikon 60 mm f/2.8 lens at 2000 frames per second.

A sample of about 25 mm³ was loaded using a syringe between the 4 mm plates of the instrument, making sure that it was totally homogeneous with no bubbles within the sample. The initial aspect ratio ($\equiv h/b$) of 0.5 was chosen based on the recommendation by Rodd et al. [40] to minimize the effects of reverse squeeze flow and sagging. A uniaxial step strain was then applied, resulting in the formation of an elongated filament. A linear stretching deformation was employed as the mode of the step strain. The stretch time was set to 50 ms. The final aspect ratio was varied with solution concentration such that filament thinning was still observed between the 4 mm plates. For example, a final aspect ratio of 2.2 was chosen for 0.2% XG in order to observe filament thinning over a timeframe of about 25 ms.

Fig. 4(a) shows the decay of the filament diameter against time for 0.2% XG which was fitted to an equation of the form:

$$D_{\text{CaBER}} = D_o \, e^{-t/3\lambda} \tag{2}$$

as recommended by Stelter and Brenn [41] for viscoelastic fluids, where D_o is the midpoint diameter following cessation of the stretch deformation and λ is a characteristic relaxation time which represents the characteristic time scale for viscoelastic stress growth in uniaxial elongational flow [40]. A linear fitting characteristic of "Newtonian-like" thinning:

$$D_{\text{CaBER}} = mt + D_o \tag{3}$$

was also fit to the data. The Trouton ratio was calculated using the equation recommended by Pelletier et al. [42]:

$$Tr = \frac{\eta_E\left(\sqrt{3}\dot{\varepsilon}\right)}{\eta(\dot{\gamma})} \tag{4}$$

with the strain rate calculated from:

$$\dot{\varepsilon} = -\frac{4}{D_o}\frac{dD_{\text{CaBER}}}{dt} \tag{5}$$

Newtonian linear thinning was observed over the entire time to breakup with a slope of about 40 mm/s. Linear fitting the last six data points prior to breakup, where the sample most closely resembles the uniform cylindrical shape used in deriving Eqs. (2) and (3), gave a slope within 10% of the global fit. Linear thinning was also observed for higher concentrations. Despite this apparent Newtonian behaviour, the Trouton ratio plotted against concentration in Fig. 4(b) confirms the non-Newtonian behaviour of this xanthan gum as the magnitude for all the concentrations studied was significantly greater than that of a Newtonian fluid, i.e. $Tr \gg 3$.

The second polymer used here was Carbopol 980 supplied by Noveon, France, in white flocculated powder form with a molecular weight of 4.00×10^6 g/mol. It is a non-toxic version of Carbopol 940 [43,44] and has been reported to show an apparent yield stress [43] when suitably neutralized. In addition to the procedure listed above for xanthan gum, therefore, the Carbopol solution was neutralized during mixing using laboratory grade 2N sodium hydroxide supplied by BDH Ltd, UK. Due to the thixotropic nature of carbopol, the solution within the flow loop was circulated at 30% of the maximum pump speed for 30 min prior to any measurements (including
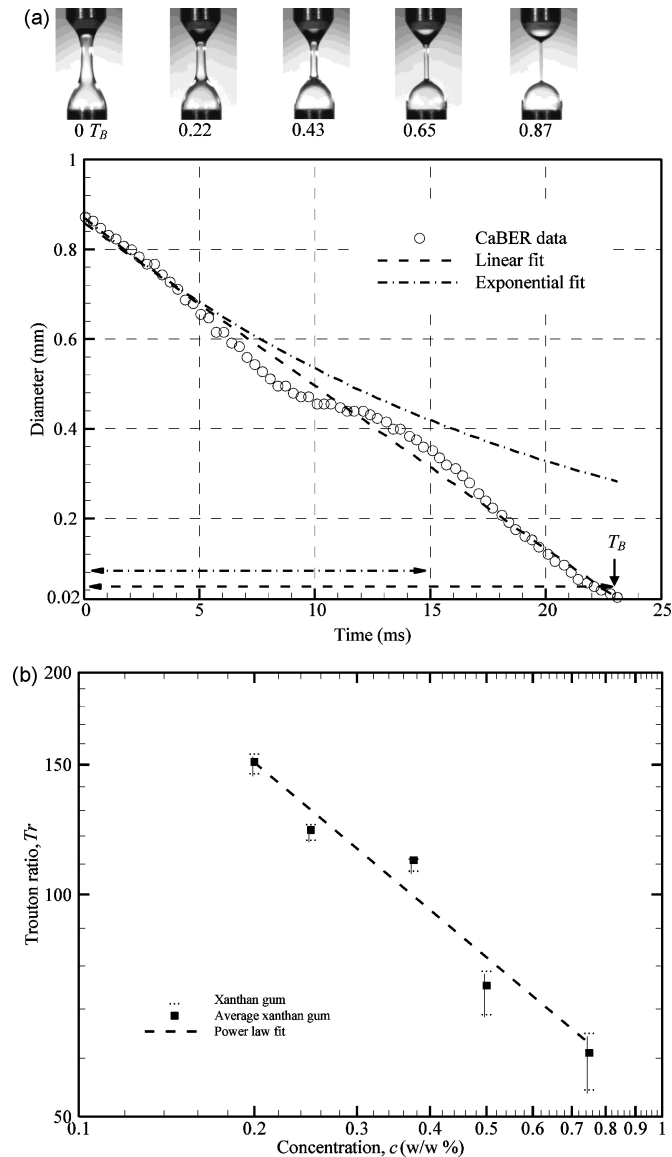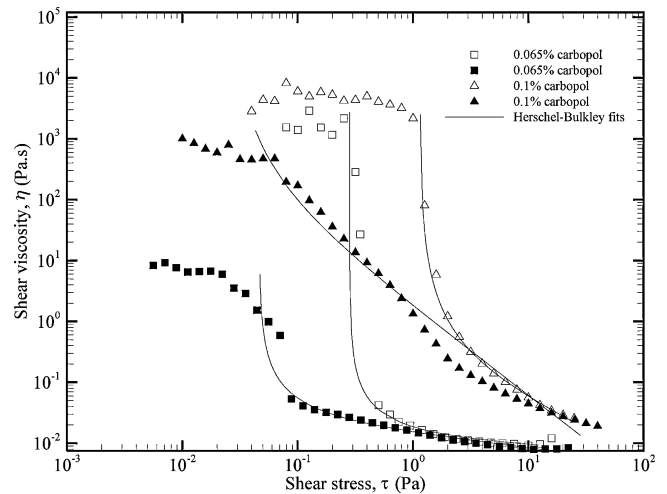
(a)

Fig. 5. Shear viscosity versus shear stress for carbopol solutions. Hollow symbols: measured using 40-mm roughened plate, filled symbols: measured using 40 mm, 2° cone and plate.

rheological tests). This pre-shear was to ensure reproducibility of the results by standardization of the solution shear history.

Complete rheological characterization of the carbopol solutions was not conducted due to the well known difficulties associated with these solutions, such as thixotropy and slip, as outlined by Presti [31]. Steady-shear measurements were only performed on 0.065% and 0.1% carbopol solutions which were prepared in the annular rig for the detailed fluid dynamic measurements. Due to wall-slip artefacts [43] which are known to exist for thickeners such as carbopol, a 40-mm stainless steel roughened parallel plate geometry was used to characterise these solutions in addition to the 40-mm, 2° cone-and-plate geometry. Fig. 5 shows the shear viscosity data against shear stress for 0.065% and 0.1% carbopol solutions measured using the cone and plate and the roughened-plate geometries. The viscosity data shows clearly that slip problems, which are most severe at low shear stresses, exist on the smooth surface of the cone-and-plate geometry which resulted in a lower apparent viscosity being measured. For the data measured using the roughened plate, where the slip effect is minimized, a very high first Newtonian region is observed at low shear stresses. Even though a real yield stress may not exist for these solutions, the abrupt viscosity transition from very high values to low values within a narrow range of shear stresses is an indication that a critical shear stress does exist above which the fluid exhibits more 'liquid-like' behaviour. The viscosity data was fitted to the
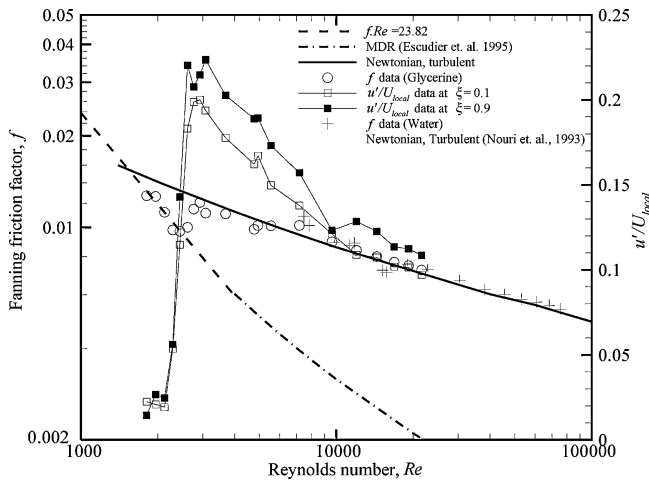
Fig. 4. (a) Filament diameter thinning as a function of time for 0.2% XG at 20 °C (arrow lines represent the time period for exponential fit $(-\cdot-)$ and linear fit $(--)$). (b) Trouton ratio versus XG concentration. The error bars represent data variations calculated from at least four measurements.

Table 1
Carreau–Yasuda parameters for xanthan gum solutions.

Concentration c (%, w/w)	Zero-shear viscosity η_o (Pa s)	Infinite-shear viscosity η_∞ (Pa s)	Constant which represents onset of shear thinning λ_{CY} (s)	Power-law exponent n	Carreau–Yasuda parameter a
0.01	1.73×10^{-3}	1.12×10^{-3}	4.93×10^{-2}	0.21	29.50
0.0124	3.15×10^{-3}	1.12×10^{-3}	9.53×10^{-2}	0.33	10.00
0.025	6.02×10^{-3}	1.12×10^{-3}	1.53×10^{-1}	0.35	4.98
0.0375	9.67×10^{-3}	1.12×10^{-3}	2.52×10^{-1}	0.37	3.35
0.05	1.97×10^{-2}	1.13×10^{-3}	3.88×10^{-1}	0.42	2.10
0.07	5.33×10^{-2}	1.33×10^{-3}	8.34×10^{-1}	0.49	1.12
0.10	2.25×10^{-1}	1.88×10^{-3}	1.77	0.60	0.57
0.15	2.16	2.67×10^{-3}	2.88	0.80	0.31
0.20	3.68	2.24×10^{-3}	2.15×10^1	0.66	0.81
0.25	9.83	3.45×10^{-3}	2.34×10^1	0.75	0.80
0.375	2.85×10^2	4.60×10^{-3}	4.14×10^2	0.81	1.47
0.5	8.41×10^2	5.25×10^{-3}	7.11×10^2	0.84	1.22
0.75	1.55×10^3	9.58×10^{-3}	1.04×10^3	0.85	0.92

Fig. 6. f–Re data for water and glycerine with u'/U_{local} levels to monitor transition for glycerine.

Herschel–Bulkley model:

$$\tau = \tau_y + K\dot{\gamma}^n \qquad (6)$$

where τ_y, K and n are, respectively, the apparent yield stress, Herschel–Bulkley constant and the power-law exponent. The fits are included in Fig. 5 and the fitting parameters are listed in Table 2.

Measurements of fluid rheology for all solutions were conducted prior to and after each LDA profile traverse to check for signs of mechanical and bacteriological degradation where a decrease of more than 5% from the initial state was taken as a sign of degradation and the fluid disposed of. The first normal-stress difference was found to be below the sensitivity of the rheometer for all polymer solutions which indicates that the fluids studied are probably only very weakly elastic in the non-linear regime, at least for the range of concentrations used here. Seeding particles (Timiron MP-1005, mean diameter approximately 5 μm, supplied by S. Blanck Ltd) were added at a concentration of 1 ppm in order to increase the signal-to-noise ratio and the data rate for the LDA measurements.

4. Pressure-drop measurements and transition identification

Fig. 6 is a plot of the Fanning friction factor, f against Reynolds number, Re for water and glycerine. Good agreement is observed with the theoretical prediction for the laminar-flow regime given

by Shah and London [45] for radius ratio $\kappa = 0.506$:

$$f = \frac{23.82}{Re} \qquad (7)$$

where Re is based on the hydraulic diameter. In the high Reynolds number, turbulent-flow regime, the data agrees well with the empirical equation given by Jones and Leung [46]:

$$\frac{1}{\sqrt{f}} = 4\log(1.343\,Re f^{1/2}) - 1.6. \qquad (8)$$

Due to its low viscosity, laminar-flow conditions were not attainable within the operating range of the flow loop for water. However, the data for glycerine shown encompasses all three flow regimes, laminar, transition and turbulent. Reasonably good repeatability was observed for the measurements with an average percentage difference of 3.7% in the friction factor.

A method initially suggested by Zakin et al. [47] and subsequently adopted by Park et al. [48] was used to detect transition from laminar to turbulent flow by plotting turbulent intensities measured at fixed radial locations against the Reynolds number. This method is especially useful for the flow of non-Newtonian fluids where transition is not always well defined in the f–Re plot. For circular pipe flows, Escudier and Presti [8] proposed that the near-wall ($r/R = 0.8$) axial rms fluctuation level is a reliable indicator of flow regime. For this study, the axial rms fluctuation level was monitored at $\xi(\equiv(r-R_i)/(R_o-R_i))$ values of 0.1 (inner-wall vicinity) and 0.9 (outer-wall vicinity). In Fig. 6, a plot of the axial rms fluctuation component normalized with the local mean velocity against the Reynolds number for glycerine, a clear demarcation from the laminar regime can be detected using this method where abrupt increases in the values are observed from a level of about 3% up to 22% of the local mean velocity. The low level axial rms fluctuations ($u'/U_{local} < 3\%$) detected within the laminar regime are a consequence of the combined noise in the LDA system and the flow loop. Normalization by the local velocity is chosen as opposed to the conventional bulk velocity normalization due to the asymmetrical nature of the velocity profile within the annular pipe. The first Reynolds number limit, Re_1, identifies the onset of transition seen as a noticeable increase in the turbulent activity while the second Reynolds number limit, Re_2, identifies the offset (end) of transition taken as being where the maximum value of turbulent intensity is reached (all value all given in Table 3). For this study Re_1 is taken as the Reynolds number where the axial rms levels exceed the 3% noise level. For glycerine, the first limit is detected at the same Reynolds number of 2100 for both the inner and the outer wall while the second limit is reached earlier for the inner wall at $Re \sim 2900$ while for the outer wall Re_2 is about 3100. Note that transition to turbu-

Table 2
Herschel–Bulkley parameters for carbopol solutions.

Concentration c (%, w/w)	Rheometer geometry	Yield stress τ_y (Pa)	Consistency index K (Pa s^n)	Power-law exponent n
0.065	Roughened plate	3.88×10^{-1}	1.10×10^{-2}	0.98
	Cone and plate	4.64×10^{-2}	3.32×10^{-2}	0.81
0.1	Roughened plate	1.14	6.19×10^{-1}	0.52
	Cone and plate	8.52×10^{-2}	1.03	0.44

Table 3
Reynolds number limits and peak axial rms fluctuation level.

Fluid	Re_1		Re_2		u'_{max}/U_{local}		Re_{crit}	β (%)	
ξ	0.1	0.9	0.1	0.9	0.1	0.9		0.1	0.9
Glycerine–water	2100	2100	2900	3100	0.20	0.22	2300	26	11
0.07% XG	3700	3700	7700	7700	0.15	0.20	6000	15	35
0.15% XG	2400	2400	14,000	11,600	0.13	0.18	6500	23	31
0.065% CARB	2000	2000	3800	3800	0.19	0.26	2800	8	15
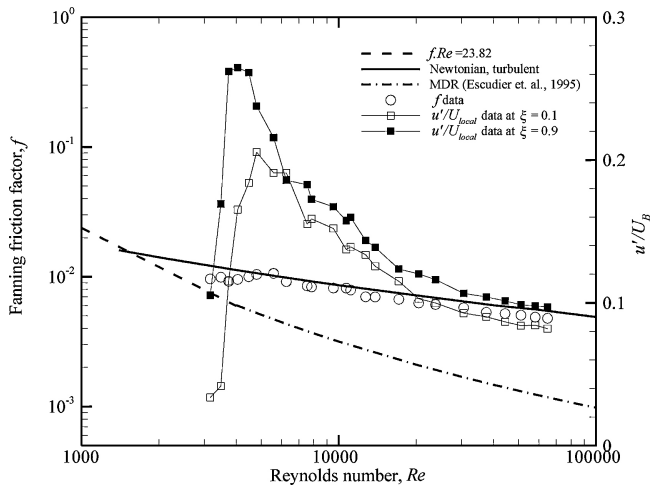
Fig. 7. f–Re and u'/U_{local} − Re data for 0.0124% XG.
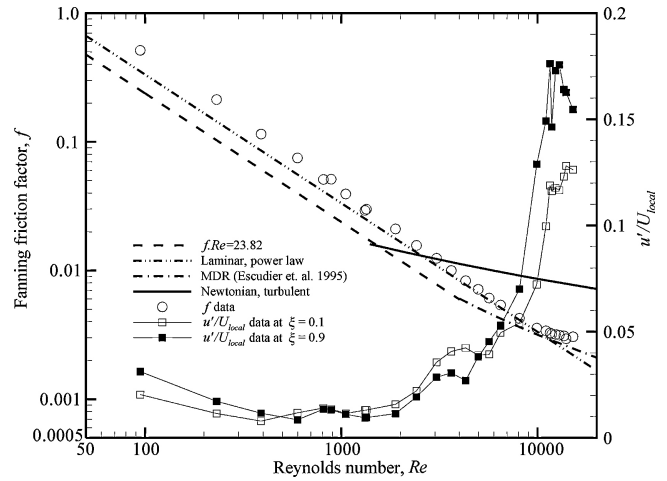
Fig. 9. f–Re and u'/U_{local} − Re data for 0.15% XG.
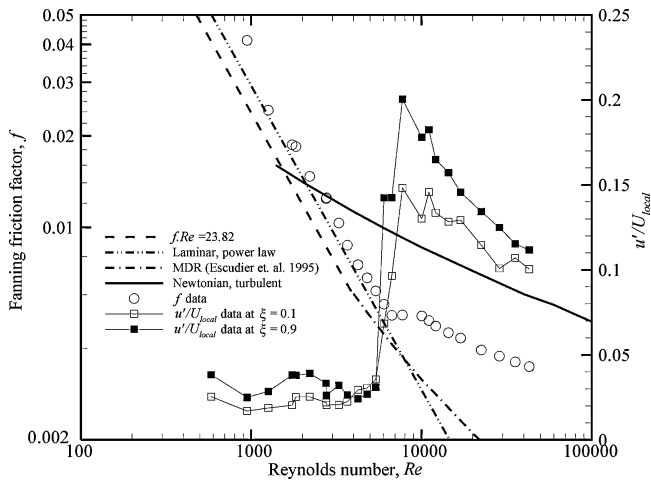

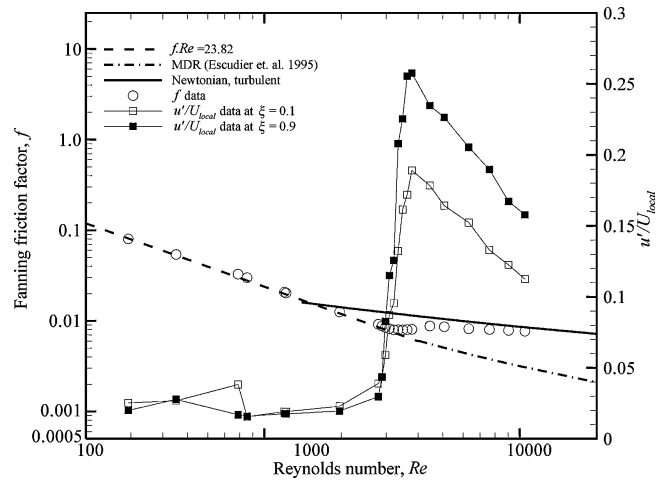**Fig. 8.** f–Re and u'/U_{local} − Re data for 0.07% XG.

Fig. 10. f–Re and u'/U_{local} − Re data for 0.065% CARBOPOL.

lence for these flows was allowed to occur naturally due to minor imperfections of the flow loop and fluctuations from the pump.

Fig. 7 shows the friction factor data for 0.0124% xanthan gum where within the flow loop operating range laminar flow was barely achievable. However at higher concentrations, 0.07% and 0.15% xanthan gum, all three flow regimes, laminar, transition and turbulent were clearly achieved, as shown in Figs. 8 and 9. The f–Re and u'/U_{local}–Re data for 0.065% carbopol shown in Fig. 10 also incorporate all three flow regimes while for 0.1% carbopol, shown in Fig. 11, the data spans only the laminar-flow regime. As was the case for the glycerine–water fluid flow, the value of Re_1 is the same at the inner and outer walls: 3700 for 0.07% xanthan gum, 2400 for 0.15% xanthan gum and 2000 for 0.065% carbopol. The offset of transition, seen as the maximum axial rms value, was also observed at the same Reynolds number for the inner and outer walls except for 0.15% xanthan gum. In Figs. 8–10, Re_2 values were found to be higher for the more shear-thinning fluids indicating later transition offset and subsequently a wider Reynolds number range for the transitional flow regime. Table 3 lists all the Reynolds number limits as determined from the near-wall turbulent-intensity measurements and also the peak values of the turbulence intensities for all fluids. It is interesting to note that these peak values decrease with increasing shear-thinning.

For the Newtonian and polymer flows, time traces of the axial velocity at ξ locations of 0.1 and 0.9 for various Reynolds numbers
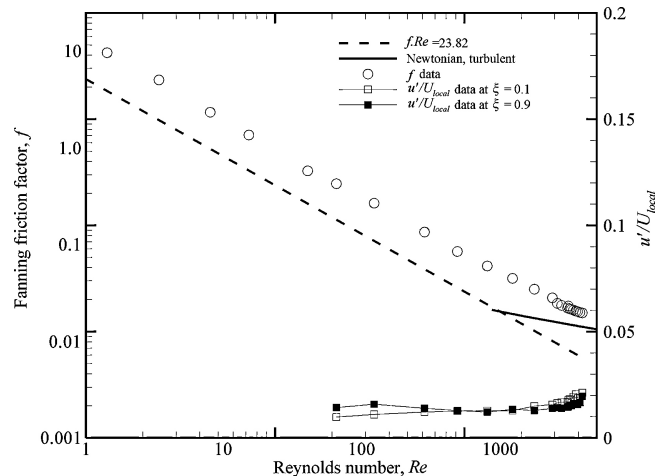

Fig. 11. f–Re and u'/U_{local}–Re data for 0.1% CARBOPOL.

spanning the three flow regimes were also monitored (although not measured at the two locations simultaneously). Fig. 12 shows the time traces for the Newtonian fluid, glycerine–water. The plots show that the flow is completely laminar for $Re = 2000$ and at $Re = 2300$ spikes are detected at both locations. The velocity spikes seen from the time traces are not typical of the puffs and slugs
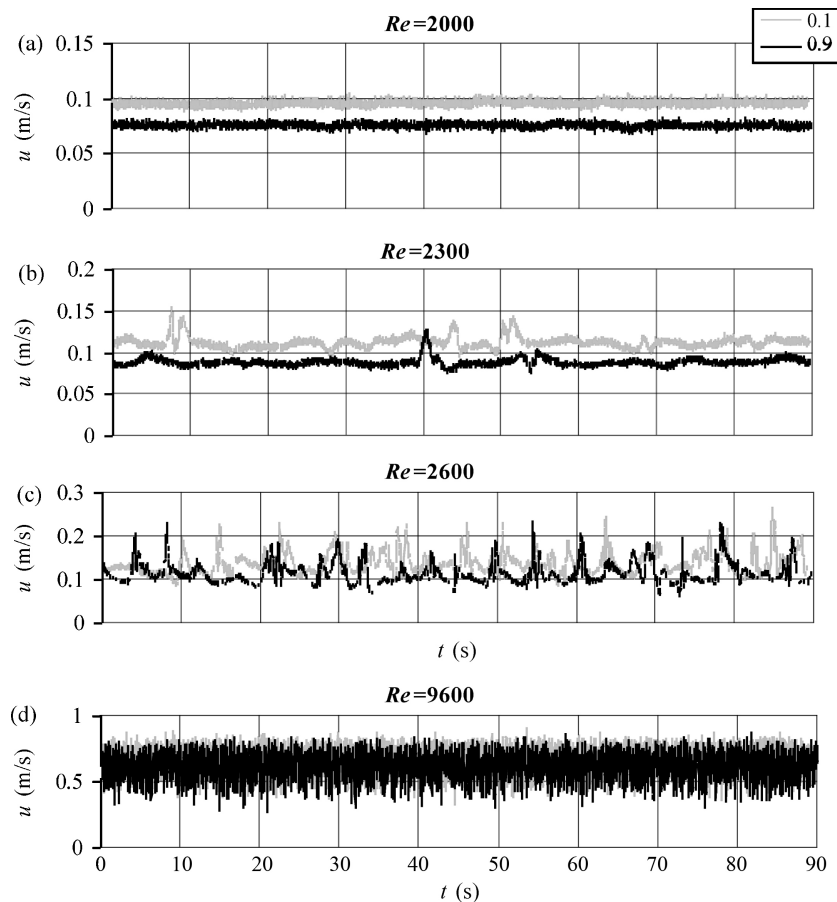
Fig. 12. Time series of the axial velocity at $\xi = 0.1$ and 0.9 for glycerine–water.

observed in pipe flow by Wygnanski and Champagne [49] and Rubin et al. [50]. The signals appear to be more complex with combinations of high- and low-amplitude spikes. The number of spikes further increases as the Reynolds number is increased to 2600. Even higher increases in Re results in more complex behaviour resembling that normally observed in fully developed turbulent flow.

In order to attempt to quantify the degree of turbulence at the onset of the transition region a method known as the $\bar{u}$ method [51] is utilized where a time ratio is defined such that:

$$\beta = \frac{\Delta t_{\text{turbulent}}}{\Delta t_{\text{total}}}\%\tag{9}$$

where $\Delta t_{\text{turbulent}}$ is taken as the total time for which spikes occur in the time trace plot over a period Δt_{total}. A spike is considered to have occurred within the time trace if the peak velocity is different by more than 15% of the local mean velocity, U_{local}. Within the laminar regime, e.g. at $Re = 2000$, the velocity varies within $\pm 15\%$ of the U_{local} but no obvious spikes are observed.

At the onset of transition for glycerine at $Re = 2300$, the time ratio for the inner wall was found to be $\beta = 26\%$ which is higher than that of the outer wall ($\beta = 11\%$). As the time ratio represents the intermittency within the flow, it can be regarded as a direct measure of how transitional the flow is. Hence, for the Newtonian fluid, the inner-wall flow has a higher degree of turbulence than that near the outer wall at the start of transition. This observation is in agreement with the behaviour predicted by the theoretical stability analysis by Hanks and Bonner [13]. At higher Reynolds numbers, the occurrence of spikes is more frequent with higher velocity fluctuations; the assessment of the time ratio becomes somewhat subjective and subject to a high degree of uncertainty.

Fig. 13 shows the time traces for 0.07% xanthan gum at various Reynolds numbers. The velocity data at $Re = 4300$ is essentially steady indicating laminar flow. At $Re = 6000$, the flow close to the inner wall is clearly unsteady but with no distinct spikes whereas high-amplitude (>50% of local mean velocity) spikes are seen for the flow close to the outer wall. This inner wall unsteadiness could be a consequence of the high amplitude spikes occurring for the flow closer to the outer wall, i.e. mass conservation enforcing changes in velocity near the inner wall but the flow remains laminar. The β values are 15% and 35% for the inner and the outer walls, respectively, indicating more turbulent activity near the outer wall. This observation suggests that the flow close to the outer wall becomes transitional earlier than the flow close to the inner wall in marked contrast to the corresponding Newtonian case. The number of high amplitude spikes increases with Reynolds number and at $Re = 28{,}700$ the flow is fully turbulent. Similar characteristics were observed for 0.15% xanthan gum and 0.065% carbopol (not shown) with the first trace of turbulence found at $Re_{\text{crit}} = 6500$ and β values of 23% and 31% on the inner and outer walls for 0.15% xanthan gum and $Re_{\text{crit}} = 2800$ for 0.065% carbopol with time ratios of 8% for the inner wall and 15% for the outer wall (see Jaafar [52] for complete details). Table 3 lists the critical Reynolds numbers obtained from the time traces and the time ratios of the flow close to the inner and outer wall at the critical Reynolds numbers.

5. Mean axial velocity measurements

Fig. 14 shows the mean axial velocity profile for glycerine–water at several Reynolds numbers spanning the three flow regimes. The velocity profile within the laminar regime at $Re = 2000$ is in good
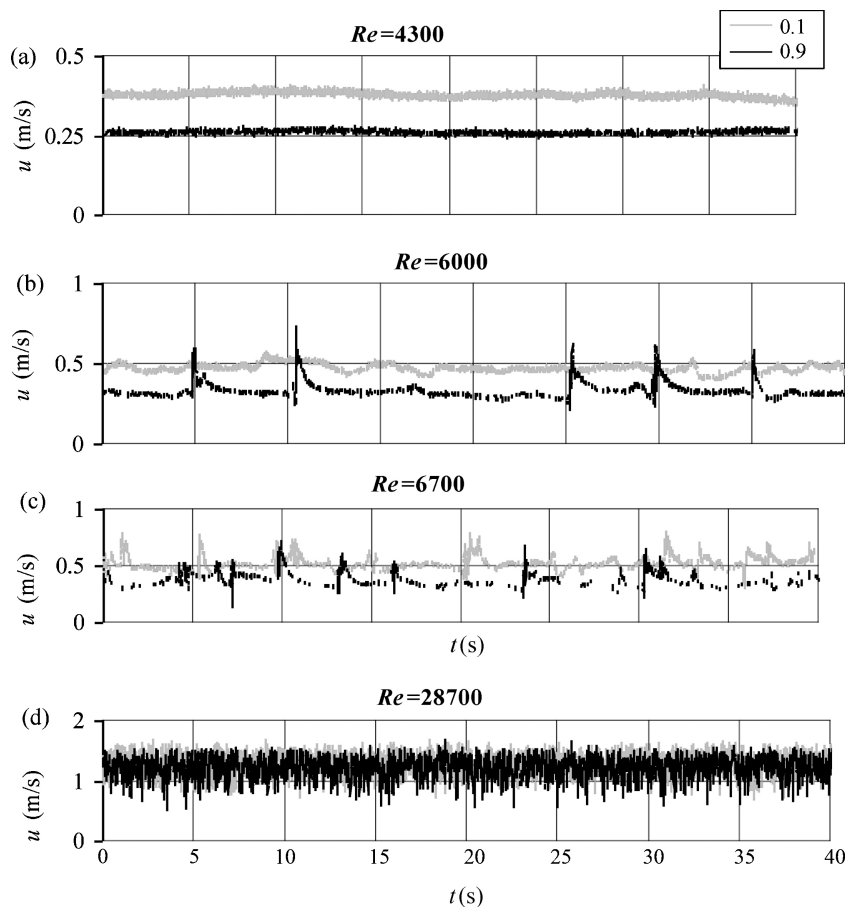
Fig. 13. Time series of the axial velocity at $\xi = 0.1$ and 0.9 for 0.07% XG.

agreement with the theoretical profile. Even though spikes were detected in the time trace at $Re = 2300$, the mean velocity profile remained essentially unchanged and agrees well with the theoretical laminar profile. At both Reynolds numbers, the velocity ratios of the maximum velocity to the bulk velocity are within the experimental uncertainty with the theoretical value of 1.51. Deviations from the theoretical laminar profile are observed at $Re = 2600$ where a slight shift towards the outer wall in the location of maximum

Fig. 14. Velocity profiles for glycerine–water at different Reynolds numbers within the laminar-, transitional- and turbulent-flow regimes, including the analytical profile for laminar flow of a Newtonian fluid (continuous lines).

velocity is also observed consistent with the higher number of turbulence spots observed at this Reynolds number. As the Reynolds number is further increased, the shape of the velocity profiles tends to what would be expected of turbulent flow: a progressively flatter central region with an increase of the velocity gradient near the walls. The ratios of the maximum velocity to the bulk velocity at these Reynolds numbers are 1.28 ($Re = 2900$), 1.24 ($Re = 3700$) and 1.15 ($Re = 9600$) respectively.
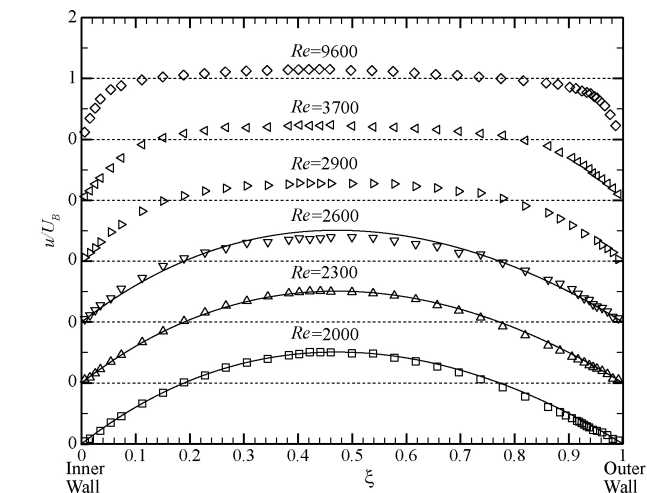
For the 0.07% xanthan gum solution the mean axial velocity profile within the laminar, transitional and turbulent regimes is presented in Fig. 15. The numerical solutions for laminar flow of a power-law fluid with $n = 0.61$, obtained using Fluent v6.1.22, are also included for comparison. As expected for a shear-thinning fluid, the ratio of maximum velocity to bulk velocity within the laminar-flow regime ($U_{max}/U_B < 1.46$) is lower than the theoretical value for a Newtonian fluid ($U_{max}/U_B = 1.51$). Fairly good agreement within the laminar-flow regime is obtained with the numerical results even at $Re = 6700$ where spikes are present in the time trace plot (Fig. 13). However, due to the flat nature of the velocity profiles within the three flow regimes, it is difficult to determine the exact location of the maximum velocity. At the higher concentration of xanthan gum (0.15%), Fig. 16, the mean velocity profile coincides with that of the numerical data with $n = 0.45$ even up to $Re = 8100$ when spikes are again present in the time trace. At $Re = 15,000$ where individual spikes could no longer be distinguished, the calculated profile for laminar flow failed to predict accurately the profile. The lower value of n for this fluid indicates greater shear thinning of the higher concentration solution which results in flatter profiles, i.e. a slightly smaller ratio of maximum velocity to bulk velocity, when compared to 0.07% xanthan gum.
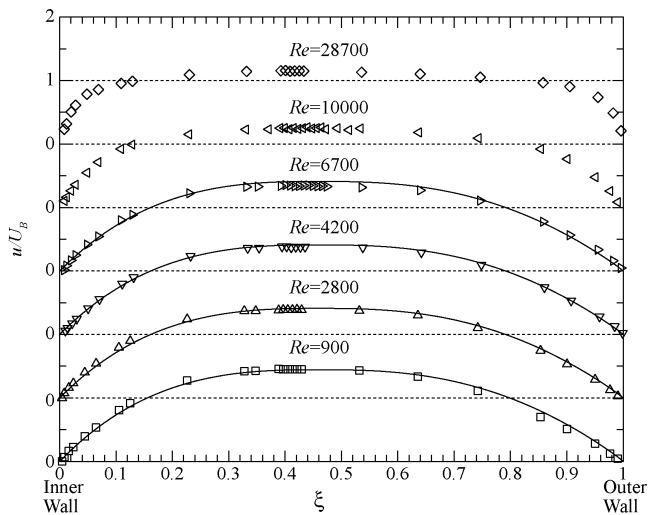
Fig. 15. Velocity profiles for 0.07% XG at different Reynolds numbers within the laminar-, transitional- and turbulent-flow regimes, including the numerical data from Fluent for laminar flow of a power-law fluid with $n = 0.61$ (continuous lines).
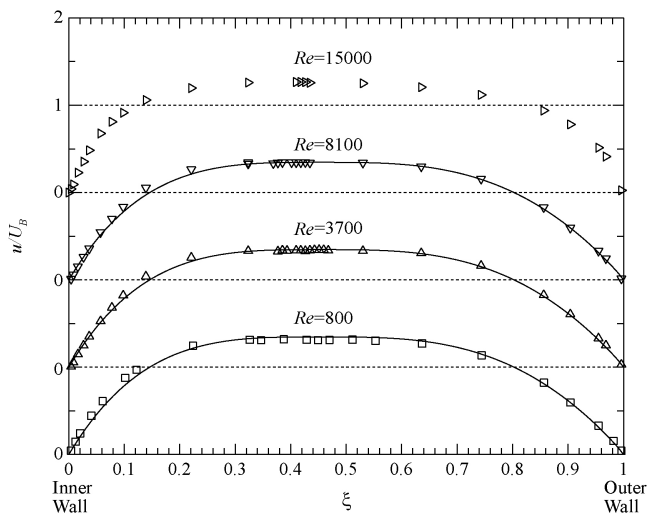

Fig. 16. Velocity profiles for 0.15% XG at different Reynolds numbers within the laminar-, transitional- and turbulent-flow regimes, including the numerical data from Fluent for laminar flow of a power-law fluid with $n = 0.45$ (continuous lines).

As the yield stress is low for 0.065% carbopol, no plug region typical of a yield-stress fluid is observed for the laminar-flow profile, and therefore for conciseness, the data is not included here. However we found better agreement with numerical data for a Herschel-Bulkley fluid with the parameters obtained from the data measured in the rheometer using the smooth cone and plate geometry. If the parameters from the data measured using the roughened plate are used in the numerical simulations, poorer agreement is observed with the experimental data. These results would seem to indicate that within the annular flow loop wall depletion, i.e. a thin layer of essentially solvent near the wall, of the carbopol solution does indeed take place. The low yield stress has no significant effect on the transition to turbulence as the behaviour is similar to that of the non yield-stress shear-thinning fluids. The location of maximum velocity within the laminar and transitional flow regimes was found to be approximately $\xi = 0.44$. However, as the Reynolds number approaches the fully-turbulent regime, the velocity profile becomes progressively flatter and it becomes difficult to determine if the location of maximum velocity has in fact shifted. For 0.1% carbopol, the turbulent-flow regime was not attainable within the
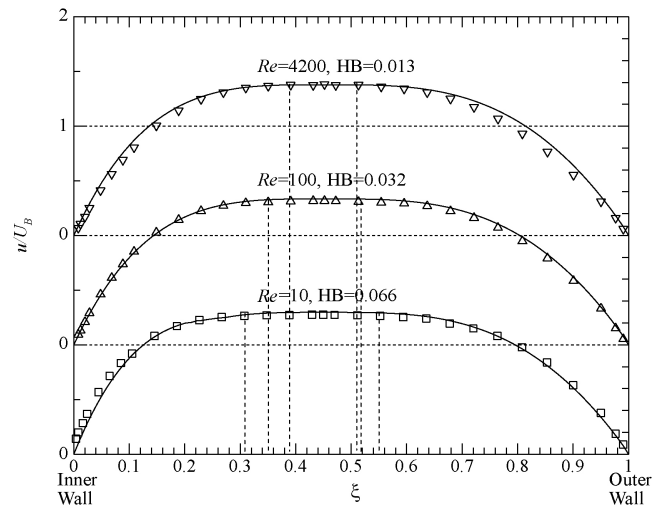

Fig. 17. Velocity profiles for 0.1% CARBOPOL at different Reynolds numbers within the laminar-flow regime, including the numerical data from Fluent for flow of a Herschel–Bulkley fluid (continuous lines). The non dimensional plug width $r_p/(R_o - R_i) = 0.25, 0.16$ and 0.11 respectively for $Re = 10, 100$ and 4200.

operating range of the flow loop. The laminar profiles as shown in Fig. 17 agree with the numerical results of the Herschel Bulkley model using the smooth cone and plate parameters suggesting that wall depletion also occurs in this flow. As can be seen in Fig. 17, the existence of the plug zone around the central region of the annular gap is more pronounced for this solution when compared to 0.065% carbopol within the laminar-flow regime as expected from the fact that the yield stress τ_y is higher for 0.1% carbopol than for the 0.065% solution. As the Reynolds number is further increased within the laminar regime, the extent of the plug region reduces due to the higher viscous shear stresses [10], with the profiles also becoming less flat with the ratio of maximum velocity to the bulk velocity found to be increasing with Reynolds number.

6. Mean flow and turbulence statistics for fully-turbulent flow

Axial-velocity profiles for water together with the Reynolds normal-stress components have been measured for three different Reynolds numbers using the "slit module" positioned 96.6 D_H downstream of the pipe entrance. As we discuss below, the use of the slit module for Newtonian fluid flow at Reynolds numbers greater or equal to 30,000 was successful but for lower Reynolds number Newtonian-fluid flow and for all the non-Newtonian fluid flows, the slit module was found to have an unacceptably large effect on the turbulent velocity field and could not be used. The mean axial velocity profiles normalized with the bulk velocity for the three Reynolds numbers are plotted in Fig. 18, together with the measurement at $Re = 9900$ where no reliable measurement of Reynolds shear stress could be made using the slit module. Data obtained by Nouri et al. [15] for a concentric annulus with radius ratio 0.5 for a Newtonian fluid at $Re = 26,600$ are also shown for comparison. Note that the data of Nouri et al. [15] has been rescaled by 6% to match the bulk velocity from the flowrate obtained through the process of integration of the velocity profiles as shown to be necessary by Chung et al. [16]. Flatter profiles are observed with increasing Reynolds number with the location of maximum velocity found to be located closer to the inner pipe wall at a non-dimensional location of $\xi = 0.44$ for all Reynolds numbers. This location is displaced by less than 1% from the location of the zero shear stress, which is within the experimental uncertainty of the determination of both locations, as determined from the Reynolds
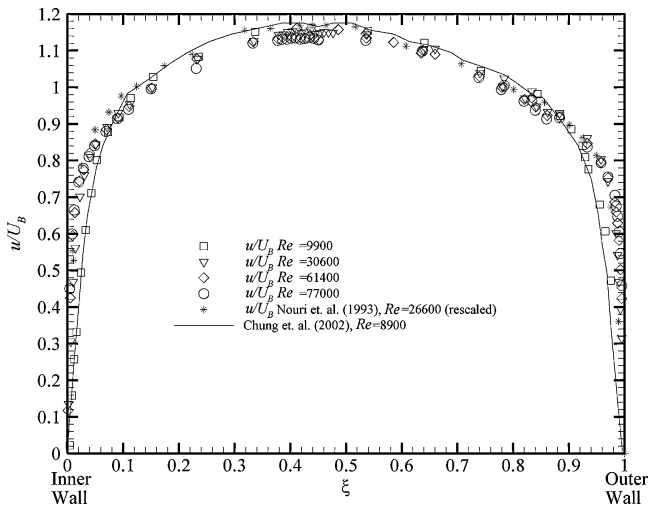
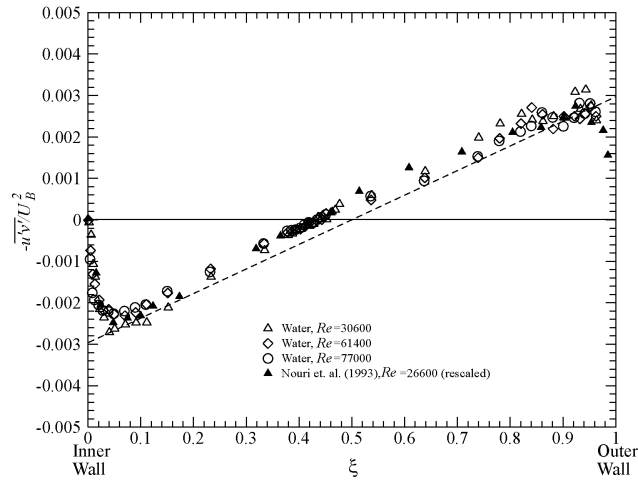**Fig. 18.** Normalized mean velocity distribution at various Reynolds numbers for water.

Fig. 19. Reynolds shear stress values normalized with the bulk velocity for water at various Reynolds numbers. A dotted line is included to show the theoretical total shear stress assuming the same shear stress on the inner and outer walls.

Fig. 20. Mean velocity distribution for water in wall coordinates. (—) $u^+ = y^+$; (---) $u^+ = 2.5 \ln y^+ + 5.5$; (-·-) $u^+ = 2.5 \ln y^+ + 4.9$ (Clauser); (□) inner wall, $Re = 9900$; (■) outer wall, $Re = 9900$; (△) inner wall, $Re = 30,600$; (▲) outer wall, $Re = 30,600$; (◇) inner wall, $Re = 61,400$; (♦) outer wall, $Re = 61,400$; (○) Inner wall, $Re = 77,000$; (v) outer wall, $Re = 77,000$.

Fig. 21. Mean velocity distribution for 0.0124% XG in wall coordinates. (—) $u^+ = y^+$; (---) $u^+ = 2.5 \ln y^+ + 5.5$; (-·-) $u^+ = 2.5 \ln y^+ + 4.9$ (Clauser); (□) 0.0124% inner wall, $Re = 10,600$, $DR = 3.2\%$; (■) 0.0124% outer wall, $Re = 10,600$, $DR = 3.2\%$; (△) 0.0124% inner wall, $Re = 30,300$, $DR = 10.3\%$; (▲) 0.0124% outer wall, $Re = 30,300$, $DR = 10.3\%$; (◇) 0.0124% inner wall, $Re = 57,600$, $DR = 11.6\%$; (♦) 0.0124% Outer wall, $Re = 57,600$, $DR = 11.6\%$.

shear-stress data plotted in Fig. 19. Since the location of maximum velocity cannot be distinguished from the location of zero shear stress, r_{max} is taken as both the location of maximum velocity and zero stress for all the fluids investigated here, as Nouri et al. did for their CMC results, where measurements of the Reynolds shear stresses were not possible.

Fig. 20 shows the mean flow data of water in wall coordinates (i.e. $u^+ (\equiv u/u_\tau)$ against $y^+ (\equiv \rho y u_\tau / \eta_W)$ for all Reynolds numbers. The friction velocity, u_τ was calculated using the wall shear stresses at the inner and outer walls. These wall shear stresses were calculated using the pressure-drop measurements and the zero shear stress location, in our case we assume $r_{\tau=0} = r_{max}$, using the equations below [17,15]:

$$\begin{aligned} \tau_o &= -\left(\frac{\Delta p}{L}\right)\left[\frac{R_o^2 - r_{\tau=0}^2}{2R_o}\right] \\ \tau_i &= -\left(\frac{\Delta p}{L}\right)\left[\frac{r_{\tau=0}^2 - R_i^2}{2R_i}\right] \end{aligned} \qquad (10)$$

The limited data close to the walls shown in Fig. 20 are in good agreement with that expected for the viscous sublayer (i.e. $y^+ < 10$, $u^+ = y^+$). In the turbulent core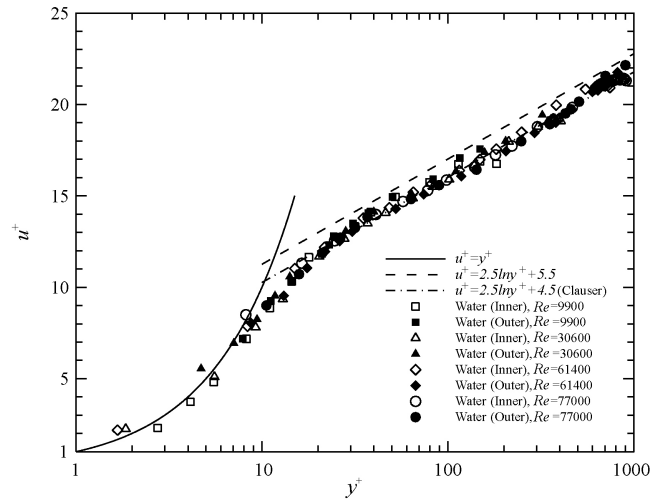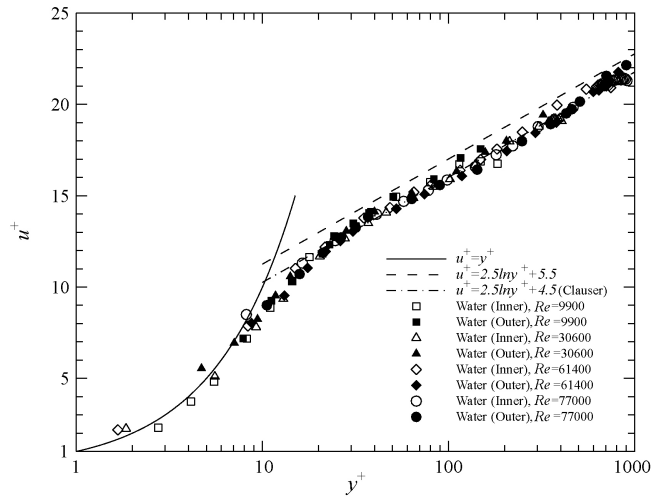 region, the data for the inner and the outer walls collapse, in agreement with the log law equation with the constant proposed by Clauser [53], as opposed to the log-law constant which is applicable to circular pipe flows [54].

Turbulent-intensity measurements were also conducted for 0.0124% and 0.07% xanthan gum. As has been established in many previous studies [31,55,56,7], amongst others, the effects of drag reduction are mainly observed in the regions close to the walls where differences are observed in peak magnitudes and locations of the fluctuation components in relation to those for a Newtonian fluid. As a consequence of these near-wall effects, in what follows wall coordinates are used to highlight this importance.

Fig. 21 shows the mean flow data in wall coordinates for 0.0124% xanthan gum. The xanthan gum data in the viscous sublayer follows $u^+ = y^+$ as expected. In the turbulent core region, the data are shifted upward from but remain parallel to the line representing data for a Newtonian fluid. The upshift is clear evidence of drag reduction. At the lowest measured Reynolds number, where the drag reduction
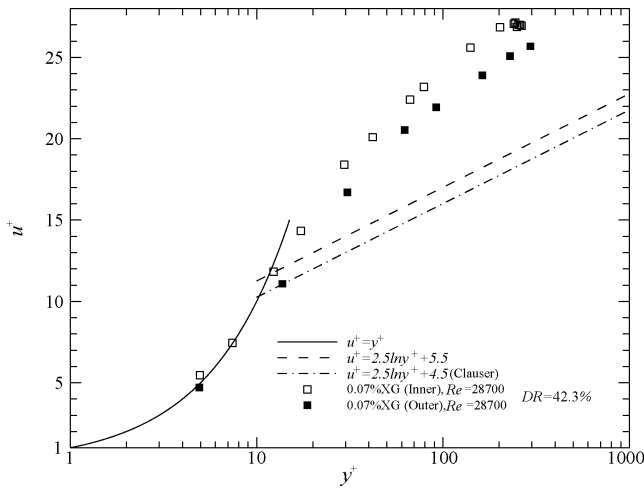
Fig. 22. Mean velocity distribution for 0.07% XG in wall coordinates. (—) $u^+ = y^+$; (- - -) $u^+ = 2.5 \ln y^+ + 5.5$; (-·-) $u^+ = 2.5 \ln y^+ + 4.9$ (Clauser); (□) 0.07% inner wall, $Re = 28,700$, DR = 42.3%; (■) 0.07% outer wall, $Re = 28,700$, DR = 42.3%.
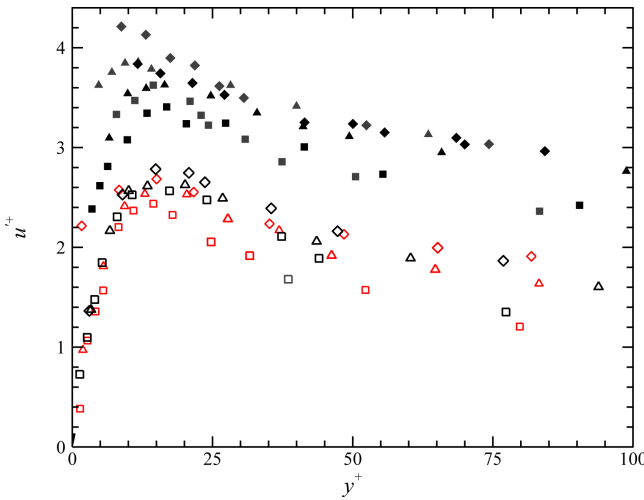

Fig. 24. Axial rms fluctuation levels in wall coordinates for water and 0.07% XG. (outer wall data upshifted on u'^+ axis by 1 wall unit). (△) Water (inner), $Re = 30,600$, $u'^+_{max} = 2.53$; (▲) water (outer), $Re = 30,600$, $u'^+_{max} = 2.86$; (△) 0.07% XG (inner), $Re = 28,700$, $u'^+_{max} = 3.16$; (▲) 0.07% XG (outer), $Re = 28,700$, $u'^+_{max} = 2.96$. (For interpretation of the references to colour in this figure legend, the reader is referred to the web version of the article.)

Fig. 23. Axial rms fluctuation levels in wall coordinates for water and 0.0124% XG. (outer wall data upshifted on u'^+ axis by 1 wall unit). (□) Water (inner), $Re = 9900$, $u'^+_{max} = 2.44$; (■) water (outer), $Re = 9900$, $u'^+_{max} = 2.63$; (△) water (inner), $Re = 30,600$, $u'^+_{max} = 2.53$; (▲) water (outer), $Re = 30,600$, $u'^+_{max} = 2.86$; (◇) water (inner), $Re = 61,400$, $u'^+_{max} = 2.68$; (◆) water (outer), $Re = 61,400$, $u'^+_{max} = 3.21$; (□) 0.0124% XG (inner), $Re = 10,600$, $u'^+_{max} = 2.57$; (■) 0.0124% XG (outer), $Re = 10,600$, $u'^+_{max} = 2.41$; (△) 0.0124% XG (inner), $Re = 30,300$, $u'^+_{max} = 2.63$; (▲) 0.0124% XG (outer), $Re = 30,300$, $u'^+_{max} = 2.63$; (◇) 0.0124% XG (inner), $Re = 57,600$, $u'^+_{max} = 2.78$; (◆) 0.0124% XG (outer), $Re = 57,600$, $u'^+_{max} = 2.84$. (For interpretation of the references to colour in this figure legend, the reader is referred to the web version of the article.)

Fig. 25. Radial rms fluctuation levels in wall coordinates for water and 0.0124% XG. (outer wall data upshifted on u'^+ axis by 1 wall unit). (□) Water (inner), $Re = 9900$, $v'^+_{max} = 0.83$; (■) water (outer), $Re = 9900$, $v'^+_{max} = 0.92$; (△) water (inner), $Re = 30,600$, $v'^+_{max} = 0.99$; (▲) water (outer), $Re = 30,600$, $v'^+_{max} = 1.08$; (◇) water (inner), $Re = 61,400$, $v'^+_{max} = 1.07$; (◆) water (outer), $Re = 61,400$, $v'^+_{max} = 1.18$; (□) 0.0124% XG (Inner), $Re = 10,600$, $v'^+_{max} = 0.70$; (■) 0.0124% XG (outer), $Re = 10,600$, $v'^+_{max} = 0.72$; (△) 0.0124% XG (inner), $Re = 30,300$, $v'^+_{max} = 0.85$; (▲) 0.0124% XG (outer), $Re = 30,300$, $v'^+_{max} = 0.90$; (◇) 0.0124% XG (inner), $Re = 57,600$, $v'^+_{max} = 0.92$; (◆) 0.0124% XG (outer), $Re = 57,600$, $v'^+_{max} = 1.06$. (For interpretation of the references to colour in this figure legend, the reader is referred to the web version of the article.)

is only about 3.2%, the outer wall data lie close to the line for a Newtonian fluid and are progressively upshifted with higher Reynolds number. Complete collapse of the inner- and outer-wall data only occurs at DR ≈ 12%. These observations suggest that the initial contribution of drag reduction comes from the inner wall where the wall shear stress is higher than on the outer wall. At even higher levels of drag reduction, seen in Fig. 22 for 0.07% xanthan gum measured at $Re = 28,700$ where DR = 42.3%, both the inner and outer walls data are no longer parallel shifted from the Newtonian line, as expected for high drag-reducing flows [55]. The outer wall profile is lower than the inner wall data indicating that the inner wall flow contributes more to the overall drag-reduction effect (assuming, of course, that the inner:outer split of pressure drop implied by Eq. (10) is correct).
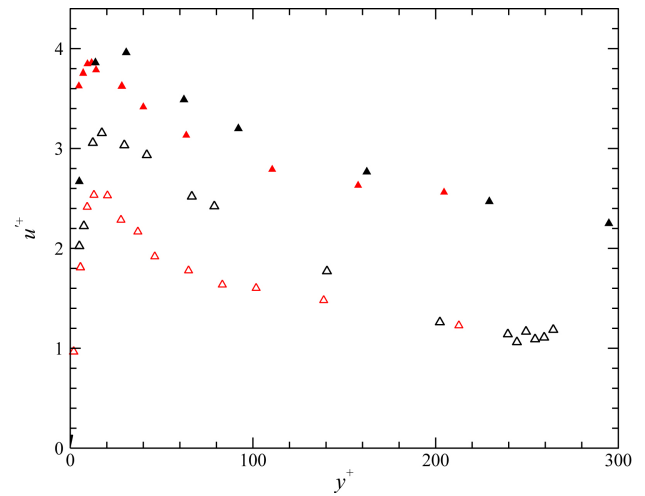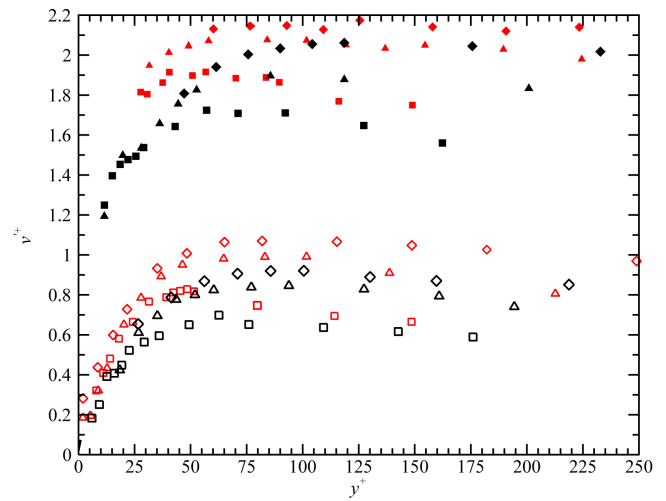
Normalizing the axial rms fluctuation component with the friction velocity, as done in Fig. 23, highlights an interesting effect (note: the outer wall data in Figs. 23–26 is upshifted on the u'^+ axis by one wall unit to separate the data). Suppressions can be observed for 0.0124% xanthan gum at all Reynolds numbers for data measured near the outer wall while a slight increase is seen on the inner wall peak values. For the inner wall peak values the differences are small and essentially within the experimental uncertainty although the trend is consistent across all the Reynolds numbers. At even higher levels of drag reduction (DR = 42.3% for 0.07% xanthan gum in Fig. 24), an increase in the peak levels is observed at both walls.
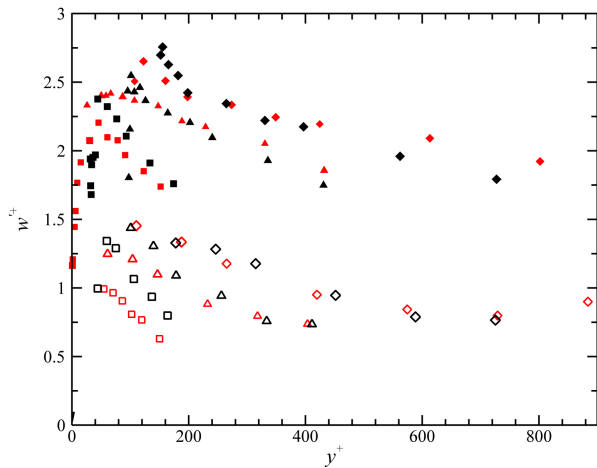
Fig. 26. Tangential rms fluctuation levels in wall coordinates for water and 0.0124% XG (outer wall data upshifted on u'^+ axis by 1 wall unit). ($\square$) Water (inner), $Re = 9900$, $w'^+_{max} = 0.99$; ($\blacksquare$) water (outer), $Re = 9900$, $w'^+_{max} = 1.20$; ($\triangle$) water (inner), $Re = 30,600$, $w'^+_{max} = 1.25$; ($\blacktriangle$) water (outer), $Re = 30,600$, $w'^+_{max} = 1.42$; ($\lozenge$) water (inner), $Re = 61,400$, $w'^+_{max} = 1.45$; ($\blacklozenge$) water (outer), $Re = 61,400$, $w'^+_{max} = 1.65$; ($\square$) 0.0124% XG (inner), $Re = 10,600$, $w'^+_{max} = 1.34$; ($\blacksquare$) 0.0124% XG (outer), $Re = 10,600$, $w'^+_{max} = 1.38$; ($\triangle$) 0.0124% XG (inner), $Re = 30,300$, $w'^+_{max} = 1.44$; ($\blacktriangle$) 0.0124% XG (outer), $Re = 30,300$, $w'^+_{max} = 1.55$; ($\lozenge$) 0.0124% XG (inner), $Re = 57,600$, $w'^+_{max} = 1.33$; ($\blacklozenge$) 0.0124% XG (outer), $Re = 57,600$, $w'^+_{max} = 1.76$. (For interpretation of the references to colour in this figure legend, the reader is referred to the web version of the article.)

Fig. 27. Radial rms fluctuation levels in wall coordinates for water and 0.07% XG. ($\triangle$) Water (inner), $Re = 30,600$, $v'^+_{max} = 0.99$; ($\blacktriangle$) water (outer), $Re = 30,600$, $v'^+_{max} = 1.08$; ($\triangle$) 0.07% XG (inner), $Re = 28,700$, $v'^+_{max} = 0.63$; ($\blacktriangle$) 0.07% XG (outer), $Re = 28,700$, $v'^+_{max} = 0.66$. (For interpretation of the references to colour in this figure legend, the reader is referred to the web version of the article.)
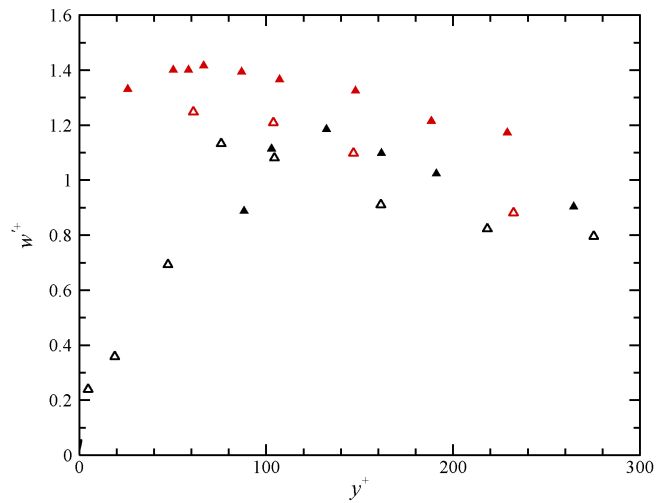

Fig. 28. Tangential rms fluctuation levels in wall coordinates for water and 0.07% XG. ($\triangle$) Water (inner), $Re = 30,600$, $w'^+_{max} = 1.25$; ($\blacktriangle$) water (outer), $Re = 30,600$, $w'^+_{max} = 1.42$; ($\triangle$) 0.07% XG (inner), $Re = 28,700$, $w'^+_{max} = 1.13$; ($\blacktriangle$) 0.07% XG (outer), $Re = 28,700$, $w'^+_{max} = 1.18$. (For interpretation of the references to colour in this figure legend, the reader is referred to the web version of the article.)
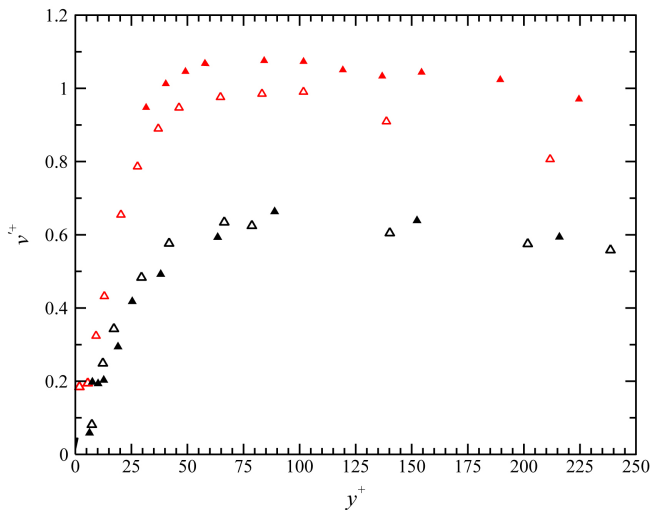

Fig. 29. Peaks of axial, radial and tangential fluctuation components normalized with the bulk velocity, U_B, plotted against drag reduction ($\square$) current study, ($\triangle$) CMC [15], ($\lozenge$) CMC, XG, LAPONITE/CMC [24]. Red: u'/U_B; green: v'/U_B; blue: w'/U_B; hollow symbols: inner wall; filled symbols: outer wall). (For interpretation of the references to colour in this figure legend, the reader is referred to the web version of the article.)

The radial rms fluctuation levels for 0.0124% xanthan gum, shown in Fig. 25, are globally much lower than that for water. In Fig. 26 increases in the peak values are observed for the tangential component except for the peak value at the inner wall for $Re = 57,600$. For higher levels of drag reduction, as in the case for 0.07% xanthan gum, increased suppression could be seen for both the radial and tangential rms fluctuation levels when plotted in wall coordinates as shown in Figs. 27 and 28.

In Fig. 29 the peak values of the turbulent fluctuation components close to the inner and outer walls, normalized with the bulk velocity, have been plotted against level of drag reduction together with the available data from the literature for the same annulus
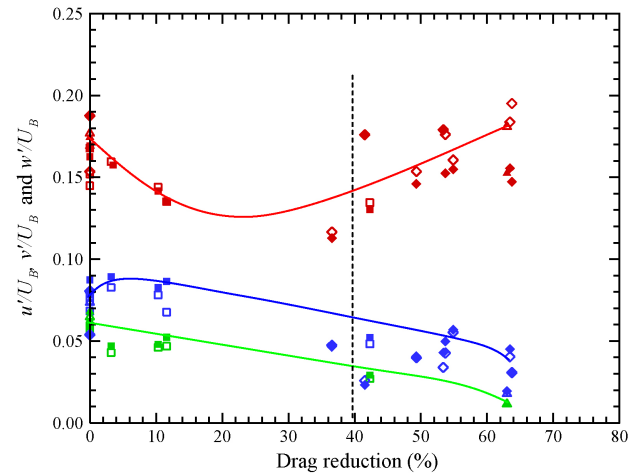
radius ratio of $\kappa \sim 0.5$ [15,24]. The lines in the figure are included to guide the reader's eye where clear trends are apparent. The limited data from the current study for the semi-rigid polymer, xanthan gum, and the data obtained from the literature show a decreasing trend below 40% drag reduction of the normalized axial peak level above which a slightly more complex but generally increasing trend is observed. A vertical dotted line is also included in the figure to demarcate these two regions. Apart from a slight increase of the normalized tangential component for DR $\leq$ 12%, decreasing normalized radial and tangential components with drag reduction can also be seen. Below 40% DR the trends are very similar to those identified by Escudier et al. [5] for flow through a rectangular duct and by Japper-Jaafar et al. [7] for pipe flow. However above 40% DR the trend in the current axial peak levels is different to the rectangular duct and pipe flow data. This discrepancy may be due to a lack of data for highly flexible high molecular weight polymers (e.g. polyethylene oxide or polyacrylamide) in the annular flow case.

Solutions of flexible polymer molecules have been shown to exhibit a different turbulent structure compared to more rigid molecules such as xanthan in complex flows for example [57].

7. Conclusions

Laminar-turbulent transition for flow of Newtonian and non-Newtonian liquids through an annular pipe was detected by monitoring the axial rms fluctuation level at fixed radial locations close to the inner and outer walls ($\xi = 0.1$ and 0.9). It was found that the Reynolds-number range for transitional flow was greater for the more shear-thinning fluids. Time traces of the mean axial velocity at these radial locations provided some insight into the nature of transition within the flow. These observations indicate that the higher shear stress on the inner wall compared to that on the outer wall does not lead to earlier transition for shear thinning and yield stress fluids as is observed for the Newtonian fluids. Though velocity variations are detected within the time traces for the flow closer to the inner wall, this effect could be a consequence of the high amplitude spikes occurring for the flow closer to the outer wall, i.e. mass conservation enforcing changes in velocity near the inner wall. The mean axial velocity indicates a slightly different behaviour for the Newtonian and polymer flow in relation to the location of maximum velocity. A shift towards the outer wall from a location of $\xi = 0.44$ could be seen within the transitional flow regime for the glycerine–water mixture due to the higher number of turbulence spots which results in further increase of the shear stress in the inner wall region compared to that in the outer wall region. The modification is a consequence of the flow adjusting to the change in momentum transport as suggested by Hanks and Bonner [13]. In contrast for the polymer flows such a shift in the location of maximum velocity is not detected and, if any, is not significant due to flattening of the velocity profiles associated with shear-thinning.

A qualitative analysis of the peak values of the turbulent fluctuation levels (normalized with U_B) in the drag-reduction study shows a decreasing trend of the axial component below 40% drag reduction. Above this drag-reduction "limit", the peak axial levels increase, generally, with drag reduction in contrast to what is observed in pipe and channel-flow studies [5,7]. Apart from a slight increase of the normalized tangential fluctuation component for DR $\leq$ 12%, the normalized radial and tangential rms fluctuating components remained below the Newtonian values for all drag-reducing flows, with the peak value decreasing with increasing drag reduction, similar to the pipe and channel-flow studies.

References

[1] R.R. Rothfus, C.C. Monrad, V.E. Senecal, Velocity distribution and fluid friction in smooth concentric annuli, Industrial and Engineering Chemistry 42 (12) (1950) 2511–2520.

[2] R.P. Chhabra, J.F. Richardson, Non-Newtonian Flow and Applied Rheology, 2nd ed., Butterworth-Heinemann, Oxford, 2008, ISBN 978-0-7506-8532-0.

[3] F.A. Seyer, A.B. Metzner, Turbulence phenomenon in drag reducing system, AIChE Journal 15 (3) (1969) 426–434.

[4] F.T. Pinho, J.H. Whitelaw, Flow of non-Newtonian fluids in a pipe, Journal of Non-Newtonian Fluid Mechanics 34 (1990) 129–144.

[5] M.P. Escudier, A.K. Nickson, R.J. Poole, Turbulent flow of viscoelastic shear-thinning liquids through a rectangular duct: quantification of turbulence anisotropy, Journal of Non-Newtonian Fluid Mechanics 160 (2009) 2–10.

[6] M.P. Escudier, S. Rosa, R.J. Poole, Asymmetry in transitional pipe flow of drag-reducing polymer solutions, Journal of Non-Newtonian Fluid Mechanics 161 (1–3) (2009) 19–29.

[7] A. Japper-Jaafar, M.P. Escudier, R.J. Poole, Turbulent pipe flow of a drag reducing, rigid "rod-like" polymer solution, Journal of Non-Newtonian Fluid Mechanics 161 (2009) 86–93.

[8] M.P. Escudier, F. Presti, Pipe flow of a thixotropic liquid, Journal of Non-Newtonian Fluid Mechanics 62 (1996) 291–306.

[9] M.P. Escudier, R.J. Poole, F. Presti, C. Dales, C. Nouar, C. Desaubry, L. Graham, L. Pullum, Observations of asymmetrical flow behaviour in transitional pipe flow of yield-stress and other shear-thinning liquids, Journal of Non-Newtonian Fluid Mechanics 127 (2005) 143–155.

[10] J. Peixinho, C. Nouar, C. Desaubry, B. Theron, Laminar transitional and turbulent flow of yield stress fluid in a pipe, Journal of Non-Newtonian Fluid Mechanics 128 (2–3) (2005) 172–184.

[11] B. Güzel, I. Frigaard, D.M. Martinez, Predicting laminar-turbulent transition in Poiseuille pipe flow for non-Newtonian fluids, Chemical Engineering Science 64 (2009) 254–264.

[12] B. Güzel, T. Burghelea, I. Frigaard, D.M. Martinez, Observations of laminar-turbulent transition of a yield stress fluid in Hagen–Poiseuille flow, Journal of Fluid Mechanics 627 (2009) 97–128.

[13] R.W. Hanks, W.F. Bonner, Transitional flow phenomena in concentric annuli, Industrial and Engineering Chemistry Fundamentals 10 (1) (1971) 105–113.

[14] K. Rehme, Turbulent flow in smooth concentric annuli with small radius ratio, Journal of Fluid Mechanics 64 (2) (1974) 263–287.

[15] J.M. Nouri, H. Umur, J.H. Whitelaw, Flow of Newtonian and non-Newtonian fluids in concentric and eccentric annuli, Journal of Fluid Mechanics 253 (1993) 617–641.

[16] S.Y. Chung, G.H. Rhee, H.J. Sung, Direct numerical simulation of turbulent concentric annular pipe flow, Part 1: Flow field, International Journal of Heat and Fluid Flow 23 (2002) 426–440.

[17] J.G. Knudsen, D.L. Katz, Fluid Dynamics and Heat Transfer, The McGraw-Hill Companies, 1958, ISBN 0882759175.

[18] R.R. Rothfus, C.C. Monrad, K.G. Sikchi, W.J. Heideger, Isothermal skin friction in flow through annular sections, Industrial and Engineering Chemistry 47 (5) (1955) 913–918.

[19] J.E. Walker, R.R. Rothfus, Transitional velocity patterns in a smooth concentric annulus, AIChE Journal 5 (1) (1958) 51–54.

[20] J.A. Brighton, J.B. Jones, Fully developed turbulent flow in annuli, Journal of Basic Engineering 86 (1964) 835.

[21] C.J. Lawn, C.J. Elliott, Fully developed turbulent flow through concentric annuli, Journal of Mechanical Engineering Science 14 (3) (1972) 195–204.

[22] K. Rehme, Turbulence measurements in smooth concentric annuli with small radius ratios, Journal of Fluid Mechanics 72 (1) (1975) 189–206.

[23] M.P. Escudier, P.J. Oliveira, F.T. Pinho, S. Smith, Fully developed laminar flow of non-Newtonian liquids through annuli: comparison of numerical calculations and experiments, Experiments in Fluids 33 (2002) 101–111.

[24] M.P. Escudier, I.W. Gouldson, D.M. Jones, Flow of shear-thinning fluids in a concentric annulus, Experiments in Fluids 18 (1995) 225–238.

[25] I.H. Gucuyener, T. Mehmetoglu, Characterization of flow regime in concentric annuli and pipes for yield-pseudoplastic fluids, Journal of Petroleum Science and Engineering 16 (1996) 45–60.

[26] I.M. Mishra, P. Mishra, Transition from laminar to turbulent flow of purely viscous non-Newtonian fluids in concentric annuli, Indian Chemical Engineer XXII (4) (1980) 39–41.

[27] P. Mishra, G. Tripathi, Transition from laminar to turbulent flow of purely viscous non-Newtonian fluids in tubes, Chemical Engineering Science 26 (1971) 915–921.

[28] R.J. Poole, Development length requirements for fully-developed laminar flow in concentric annuli, ASME Journal of Fluids Engineering 132 (6) (2009) 064501.

[29] F.M. White, Viscous Fluid Flow, The McGraw-Hill Companies, 2005, ISBN 0-071-24493-X.

[30] B.R. Munson, D.F. Young, T.H. Okiishi, Fundamentals of Fluid Mechanics, 4th ed., John Wiley and Sons, Inc., 2002, ISBN 0-471-44250-X.

[31] F. Presti, Investigation of transitional and turbulent pipe flow of non-Newtonian fluids, Ph.D. Thesis, University of Liverpool, 2000.

[32] D. Poggi, A. Porporato, L. Ridolfi, An experimental contribution to near-wall measurements by means of a special laser Doppler anemometry technique, Experiments in Fluids 32 (2002) 366–375.

[33] C. Tropea, Laser Doppler anemometry: recent developments and future challenges, Measurement Science and Technology 6 (1995) 615–619.

[34] W.J. Yanta, R.A. Smith, Measurements of turbulence-transport properties with a laser Doppler velocimeter, in: AIAA 11th Aerospace Science Meeting, 1973.

[35] K. Yasuda, R.C. Armstrong, R.E. Cohen, Shear flow properties of concentrated solutions of linear and star branched polystyrenes, Rheologica Acta 20 (1981) 163–178.

[36] M.P. Escudier, I.W. Gouldson, A.S. Pereira, F.T. Pinho, R.J. Poole, On reproducibility of the rheology of shear thinning liquids, Journal of Non-Newtonian Fluid Mechanics 97 (2001) 99–124.

[37] M. Milas, M. Rinaudo, M. Knipper, J.L. Schuppiser, Flow and viscoelastic properties of xanthan gum solutions, Macromolecules 23 (1990) 2506–2511.

[38] R. Lapasin, S. Pricl, Rheology of industrial Polysaccharides: Theory and Applications, Blackie Academic and Professional, 1995, ISBN 0 7514 0211 7.

[39] A.B. Rodd, D.E. Dunstan, D.V. Boger, Characterisation of xanthan gum solutions using dynamic light scattering and rheology, Carbohydrate Polymers 42 (2000) 159–174.

[40] L.E. Rodd, T.P. Scott, J.J. Cooper-White, G.H. McKinley, Capillary break-up rheometry of low-viscosity elastic fluids, Applied Rheology 15 (2005) 12–27.

[41] M. Stelter, G. Brenn, Elongational rheometry for the characterization of viscoelastic fluid, Chemical Engineering and Technology 25 (1) (2002) 30–35.

[42] E. Pelletier, C. Viebke, J. Meadows, P.A. Williams, A rheological study of the order-disorder conformational transition of xanthan gum, Biopolymers 59 (2001) 339–346.

[43] G.P. Roberts, H.A. Barnes, New measurements of the flow-curves for Carbopol dispersions without slip artefacts, Rheologica Acta 40 (2001) 499–503.

[44] H. Zhu, Y.D. Kim, D.D. Kee, Non-Newtonian fluids with a yield stress, Journal of Non-Newtonian Fluid Mechanics 129 (2005) 177–181.

16 *A. Japper-Jaafar et al. / J. Non-Newtonian Fluid Mech. xxx (2010) xxx–xxx*

[45] R.K. Shah, A.L. London, Laminar Flow Forced Convection in Ducts, Academic Press, New York, 1978, ISBN 0-12-020051-1.

[46] O.C. Jones, J.C.M. Leung, An improvement in the calculation of turbulent friction in smooth concentric annuli, Journal of Fluids Engineering 103 (1981) 615–623.

[47] J.L. Zakin, C.C. Ni, R.J. Hansen, Laser Doppler velocimetry studies of early turbulence, Physics of Fluids 20 (10–2) (1977) 85–89.

[48] J.T. Park, R.J. Mannheimer, T.A. Grimley, T.B. Morrow, Pipe flow measurements of a transparent non-Newtonian slurry, Journal of Fluids Engineering 111 (1989) 331–336.

[49] I.J. Wygnanski, F.H. Champagne, On transition in a pipe. Part 1. The origin of puffs and slugs and the flow in a turbulent slug, Journal of Fluid Mechanics 59 (2) (1973) 281–335.

[50] Y. Rubin, I.J. Wygnanski, J.H. Haritonidis, Further observations on transition in a pipe, in: R. Eppler, H. Fasel (Eds.), Laminar-Turbulent Transition. IUTAM Symposium Stuttgard, Germany, 1979, pp. 17–26.

[51] D.H. Zhang, Y.T. Chew, S.H. Winoto, Investigation of intermittency measurement methods for transitional boundary layer flows, Experimental Thermal and Fluid Sciences 12 (1996) 433–443.

[52] A. Jaafar, Duct flow of polymer solutions, Ph.D. Thesis, University of Liverpool, 2010.

[53] F.H. Clauser, The turbulent boundary layer, Advances in Applied Mechanics 4 (1956) 1–51.

[54] H. Tennekes, J.L. Lumley, A First Course in Turbulence, The MIT Press, 1972, ISBN 978-0-262-20019-6.

[55] M.D. Warholic, H. Massah, T.J. Hanratty, Influence of drag-reducing polymers on turbulence: effects of Reynolds number, concentration and mixing, Experiments in Fluids 27 (1999) 461–472.

[56] M.P. Escudier, F. Presti, S. Smith, Drag reduction in turbulent pipe flow of polymers, Journal of Non-Newtonian Fluid Mechanics 81 (1999) 197–213.

[57] R.J. Poole, M.P. Escudier, Turbulent flow of viscoelastic liquids through an axisymmetric sudden expansion, Journal of Non-Newtonian Fluid Mechanics 117 (2004) 25–46.